CONSTRAINTS UPON THE HISTORY OF MERIDIANI PLANUM, MARS USING SUB-KILOMETER CRATER COUNTING

By

Sharon Ellen Pitiss

RECOMMENDED:

Doug Christensen

Ken Dean

Robert Herrick

Advisory Committee Chair: Virgil Sharpton

Chair, Department of Geology and Geophysics: Mike Whalen

APPROVED:

Dean, College of Natural Science and Mathematics: Joan Braddock

Dean of the Graduate School: Susan Henrichs

April 11, 2005
Date

CONSTRAINTS UPON THE HISTORY OF MERIDIANI PLANUM, MARS USING SUB-KILOMETER CRATER COUNTING

A

THESIS

Presented to the Faculty

of the University of Alaska Fairbanks

in Partial Fulfillment of the Requirements

for the Degree of

MASTER OF SCIENCE

By

Sharon Ellen Pitiss, B.S.

Fairbanks, Alaska

May 2005

Abstract

Analysis of a surface's crater population provides information to reconstruct the geologic history of a regional surface. Therefore, the population of sub-kilometer impact craters within Meridiani Planum, Mars has been assessed to constrain the nature and origin of unique hematite-rich deposits that occur in this region. Crater size-frequency distributions were compiled for 16,540 small craters in eleven images with varying hematite concentration. Results show that a complex crater obliteration process, probably aeolian activity, has operated continuously on the Meridiani region between ~10 My and 3 Gy. More recently the surface process seems to have halted, possibly due to dune stabilization associated with a major climate shift. There is no evidence in the cratering record of an extensive, long-lived body of water that could have created the region's hematite deposits. While not required by the size-frequency distribution, some regional stripping and removal is permitted. In this case, the maximum erosional depth incurred in the last 3 Gy is limited to less than 50 meters. This is insufficient to have metamorphosed hematite as Lane et al. (2002) previously suggested. The size-frequency distributions suggest the hematite would have had to be emplaced very early in the history of Mars.

TABLE OF CONTENTS

Page

Page

LIST OF FIGURES

Page

Page

Page

LIST OF TABLES

Page

LIST OF APPENDICES

Page

ACKNOWLEDGMENTS

Thank you to my advisor Buck Sharpton and committee members Ken Dean, Doug Christensen, and Robert Herrick for their thoughtful input and time invested in making me a scientist. Thank you to John Chappelow (PhD candidate, UAF planetary science program) for countless hours of clarifying concepts throughout the years; he is really an inspiration to me. My family has been extremely supportive, especially my superhero dad. Of course my partner Lars Hansen should be thanked, but he must know that I'm only with him because his name rhymes with Mars. My Viking-esque Icelandic best friend, Sigrun Hreinsdottir, has kept me from going insane.

Funding to support this thesis project was graciously provided by NASA Mars Data Analysis Program and NASA Planetary Geology and Geophysics Program through grants (NAG5-10605, NAG5-9392, NAG5-13580) to Dr. Sharpton.

1 Introduction

1.1 Background

The Mars Global Surveyor (MGS), launched in 1996, has returned a wealth of data from its onboard instruments and continues to provide important clues to understanding the red planet. The MGS Mars Orbiter Camera (MOC) images portions of Mars at unprecedented resolution, documenting the surface effects of wind, water, ice, volcanic eruptions, tectonics, and other geologic processes. The pixel spacing of MOC narrow angle (MOC-NA) images is as precise as 1.4 m per pixel (Malin et al., 1998). The resolution is one to two times as large as the pixel spacing, therefore features as small as 4-7 meters are recognizable (Malin et al., 1998). MOC's narrow-angle camera has now examined nearly 4.5 percent of the surface of Mars, including extensive imaging of selected landing sites for surface missions. MOC also takes lower resolution, wide-angle (MOC-WA) images of the entire planet over time to enable research into the temporal changes in the atmosphere and on the surface.

1.2 Hematite Region

The Thermal Emission Spectrometer (TES), also on board MGS, detected an unusual and potentially very important spectral signature associated with a 350 km by 750 km region within Meridiani Planum (hereafter termed Meridiani) located near the meridian at 0°S, 0°W (Figure 1). Unlike the bulk of Mars, spectra of this region contain absorption features characteristic of crystalline hematite (Fe_2O_3) (Christensen et al., 2000), which are distinctly unlike basalt and basaltic andesite (Noreen et al.,

2001). Depths of the characteristic absorption features indicate that surfaces in this region contain between 10-15 wt% crystalline hematite (Christensen et al., 2000).

Meridiani is completely within unit Npl2 on Scott and Tanaka's (1986) 1:2,000,000 Geological Map of Mars; this unit is described as a subdued crater unit marked by subdued and partly buried old crater rims. Scott and Tanaka (1986) interpret this unit as thin interbedded lava flows and aeolian deposits that partly bury underlying rocks. Hynek et al. (2002) have mapped the area and labeled it P2: dark basaltic plains less than a few hundred meters thick containing hematite.

Because of the strong hematite signature uniquely associated with this region, NASA chose Meridiani as the landing site for Opportunity, one of two 2003 Mars Exploration Rovers (MER). Its main task is to explore the areas around its landing site for evidence in rocks and soils of past aqueous environments that were possibly suitable for sustaining life. To date, Opportunity rover results are essentially consistent with the above interpretations, e.g. hematite detection, layering in rocks and crater walls, and volcanic origins (Squyres et al., 2004).

On Earth, course-grained hematite is most commonly formed by precipitation from surface waters that have interacted with mafic rocks containing iron-bearing minerals. Thus, the uniqueness of the Meridiani hematite signature and its implications for long standing surface waters make this area an intriguing site for study.

1.3 The Origin of Crystalline Hematite on Mars

Christensen et al. (2000) consider five possible mechanisms for the formation of coarse-grained, crystalline hematite, all involving either chemical precipitation from near-surface waters or thermal oxidation of magnetite-rich lavas in a volcanic environment. They prefer mechanisms involving chemical precipitation from iron-rich water on the basis of the probable association with sedimentary materials, large geographic size of the hematite signature, distance from a regional heat source, and lack of evidence for extensive groundwater processes elsewhere on Mars. Noreen et al. (2001) propose a volcanogenic formation – either mineralization within the welded zone of an ignimbrite or hydrothermal enrichment of volcanic materials – based on volcanic associations, geomorphology, and comparison with Valles Marineris, which also shows a TES signature of crystalline hematite, although of much lesser extent and concentration (Christensen et al., 2000). Lane et al. (2002) believe the emissivity spectra over Meridiani indicate that the coarse, gray hematite in Meridiani is also microplaty (schistose), perhaps having undergone low-grade metamorphism due to burial. Their observations are consistent with a model where the platy, gray hematite originated as an iron oxide chemically precipitated from water on early Mars that was buried, re-crystallized to schistose (platy) hematite, and subsequently re-exposed as schistose lenses in a friable, consolidated stratigraphic unit.

Other studies have adopted and expanded upon the concept of surface waters dissolving mafic rocks containing iron-bearing minerals (e.g., Hartmann, 2001a; Kelsey et al., 2000; Lane et al., 1999; and Gilmore and Tanaka, 2002) to explain the

presence of the Meridiani hematite signature. The central tenet of all these studies is that a hematite-rich unit was emplaced (possibly precipitated onto a lakebed) during an earlier, warmer-wetter epoch of martian history. This layer was then buried by a thick mantling deposit thereby metamorphosing it to schistose hematite (also serving to protect it over time from further impact and geologic processes). Finally, the mantle has been exhumed recently to reveal the hematite-rich deposit.

1.4 Crystalline Hematite as an Indicator of Long-standing Surface Water

Kirkland et al. (2004) have shown that the inferred coarse hematite does not match the TES spectra as well as fine-grained, consolidated hematite (including closely packed fines, duricrust, ferricrete, and desert varnish). Coarse hematite is considered strong evidence for longstanding water, but it is unknown whether the role of water for formation and preservation of fine-intimate hematite on Mars is vital, which might explain the lack of other aqueous alteration minerals and hematite wind streaks in Meridiani (Kirkland 2004).

Currently, liquid water is thermodynamically unstable on Mars' surface, however valley networks and outflow channels provide incontrovertible evidence for substantial surface waters in the ancient past of Mars. The general consensus is that these landforms were produced through catastrophic release of subsurface water in response to regional heating associated with early volcanism [e.g. Carr, 1996; Kargel and Strom, 1996].

As intriguing as the transient existence of surface waters may be, such events would probably not be conducive to either the formation or evolution of primitive

martian life and therefore would not be central to NASA's astrobiology interests. However, the hematite signature revealed by TES indicates the possibility of standing water on Mars at one time. Therefore the concept of a warmer, wetter epoch in the history of Mars when atmospheric conditions may have permitted stable, liquid water on the surface has become a paradigm. The search for evidence of such an epoch has become a central theme in all aspects of Mars exploration.

2 *Objectives*

The purpose of this study is to assess the population of sub-kilometer-scale impact craters within Meridiani for information to constrain the nature and origin of the hematite-rich deposits. Impact crater size-frequency distributions were compiled for small (<1km) craters in eleven narrow-angle, high-resolution MOC-NA images, with center longitude and latitude located between 2°W and 7°W and 2°S and 3°S within Meridiani (Figure 1, Table 1). The area in Meridiani with the highest hematite concentration does not occur within the 2003 Mars Exploration Rover landing ellipse. In order to make a comparison of the cratering record in areas of differing hematite concentration, five study sites were selected within the Opportunity landing ellipse, which has a lower hematite concentration, and six of the images measured lie within the region of Meridiani that shows the strongest hematite concentration (Figure 1).

There are three main constraints that the 16,540 sub-kilometer craters measured in Meridiani will provide: (1) an estimate of the maximum allowable burial/exhumation depth in the region since the current crater population was formed, relevant to understanding whether or not the hematite has undergone burial metamorphism as proposed by Hartmann, 2001a; Kelsey et al., 2000; Lane et al., 1999; and Gilmore and Tanaka, 2002; (2) the timing of any discrete burial or erosional events; and (3) the nature of recent activity that might be modifying the hematite deposits.

3 Method

3.1 Approach to Impact Crater Studies

Impact cratering has played a fundamental role in the creation and evolution of planets. Because the rate at which craters are produced on the terrestrial planets is thought to have remained more or less constant over the last 3 Gy (Shoemaker et al., 1962), analysis of a surface's crater population is a heavily relied upon means of establishing both relative and absolute chronologies. Competing endogenic or exogenic geological processes will modify this production population in accordance with the nature, duration, and intensity of the surface process. Consequently, analysis of a surface's crater record provides helpful clues to reconstructing the geologic history of a regional surface. For example, if a surface has experienced volcanic flooding in its recent past, it might show a paucity of impact craters whose rim heights did not exceed the thickness of the lava. Many studies have reviewed modifications of the local cratering record by various resurfacing processes (Basaltic Volcanism Study Project, 1981; Chapman, 1974; Opik, 1966; Chapman and Jones, 1977; and Hartmann, 1977).

3.2 The Size-Frequency Diagram

A size-frequency distribution describes the number of craters of a given size counted and binned within a region. Two types of size-frequency distributions are in wide use (Crater Analysis Techniques Working Group, 1979; Arvidson et al., 1977): the cumulative plot and the differential (or incremental) plot. On a cumulative plot, the number of craters larger than a given diameter is plotted, while in the differential

case the number of craters between two limits, defined as a 'bin', is plotted. When a reference is made to a particular bin, its lower diameter limit is cited. In an incremental plot, the density of craters between the two limits of the bin is plotted at the midpoint diameter of the bin. Each bin is an increment of $\sqrt{2}$.

In this study, the differential approach is employed because it more clearly displays losses of craters in any particular size bin. For example, if a certain region has had some resurfacing episode that removed all craters between 125 m and 500 m in diameter, the differential plot would show an obvious downturn in that size interval, while the cumulative plot would merely flatten out, artificially smoothing the data (Hartmann, 1977).

Absolute ages have been attached to several lunar surfaces by radiometric dating of samples returned by the Apollo program. When plotted on a size-frequency distribution, the diameter distribution of the crater population on a surface of known age constitutes an isochron, or line of constant age. An example size-frequency distribution of the average lunar mare is shown in Figure 2. The slopes of isochrons are defined by the unmodified crater production rate as a function of diameter; their positions on a size-frequency distribution depend on their ages, with older isochrons located above and to the right (toward larger diameters) of younger ones. The ages of other lunar surfaces can then be estimated by comparing their crater populations to the known set of lunar isochrons.

3.3 Isochrons for Mars

Since independent radiometric age information is not available for Mars,

martian isochrons have been extrapolated to Mars from the Moon by estimating cratering rates on Mars relative to those on the Moon (Hartmann et al., 1999; 2001b). The equation for Hartmann's 3.6 Gy isochron for craters less than ~975 m (the largest craters measured in this study were less than this) is:

$$N_{3.6Gy} = 8.45X10^{-4} D^{-3.82} \quad (1)$$

where N signifies the number of craters per km^2 of a given diameter bin D. Isochrons younger than 3.0 Gy assume a constant cratering rate after a slight decline and thus their equation is:

$$N_{AGy} = 0.95\left(\frac{A_{Gy}}{3.6_{Gy}}\right) \times \left(8.45X10^{-4} D^{-3.82}\right) \quad (2)$$

where A_{Gy} is the age of the wanted isochron in billions of years. Equations (1) and (2) are published on a website (Hartmann, 2002); however, plots recently added on the website indicate that Hartmann's parameters have changed but new equations have not been published.

The isochrons defined by equations (1) and (2) are subject to much uncertainty, mainly due to problems associated with extending lunar crater production rates to Mars (Basaltic Volcanism Study Project, 1981). This uncertainty arises from effects such as differences in planetary gravity, presence of a martian atmosphere and differing impact velocities. Another source of uncertainty, and currently the subject of much debate, is the role of secondary cratering in crater production rates (McEwen, 2003; Block and Barlow, 2005). However, the exact positions of the isochrons on a

size-frequency distribution do not significantly affect our analysis because we use these isochrons primarily as points of reference to establish relative chronologies.

Systematic errors in crater counting are the result of such things as image resolution and quality effects, and subjective interpretation in identifying craters. The main source of error in crater population counts is sampling error. Sampling errors arise from estimating a population characteristic by looking at only one portion of the population rather than the entire population. The errors, ε, for the size-frequency distributions in this study are calculated from the standard sampling error formula:

$$\varepsilon = \frac{N^{0.5}}{area} \tag{3}$$

As a surface ages and becomes more and more crowded with craters, it reaches a point where, on average, each new impact effectively erases one old crater of the same size. This condition is described by a saturation line on a size-frequency distribution, given by Hartmann (2002) as:

$$N_{saturation} = 4.677X10^{-2} D^{-1.83} \tag{4}$$

Theoretically, by definition, no crater counts should exceed this line.

3.4 Importance of the sub-km crater record

Erosive and depositional processes preferentially remove smaller craters on older surfaces. Prior to the launch of MGS, the resolution of Mars photographs did not permit construction of a size-frequency distribution for craters smaller than ~1 km in diameter. With the images from the MOC, impact craters with a diameter as small as 12 meters can be discerned.

The validity of crater population studies depends upon the counting of statistically significant populations of impact craters; the larger the number of craters counted, the less important statistical effects on a size-frequency distribution become. Because small craters are produced at much higher rates, we can usually count many more small craters than larger ones in a given area, improving our statistics. We can also obtain meaningful results from much smaller surface areas. Also, due to their high production rates, small-crater populations tend to reflect much younger geological events than populations of larger craters. Erosive and depositional processes also preferentially remove small craters over larger ones, therefore such processes should be much easier to detect in counts of small craters.

3.5 MOC-NA images

The images used in this study were selected based on the following criteria (Table 1):

1) The image pixel spacing is less than 3.65 meters per pixel.
2) The image is located within the hematite signature defined by TES either within the landing ellipse of the 2003 MER or within the highest concentration of hematite (Figure 1).
3) There are no significant numbers of obvious secondary craters (smaller craters created from the ejecta of a larger crater) present in the image.
4) The images were publicly available at the time of this study.

The selected images were processed using ISIS (Integrated Software for Imagers and Spectrometers), an image processing software package used to

manipulate imagery collected by current and past NASA planetary missions. The processing includes data ingestion, radiometric correction, geometric rectification, and photometric correction (Figure 3). The final step is conversion of the image from NASA format into a bitmap to be loaded into a crater analysis program after all processing has occurred.

3.6 Crater Counting in Meridiani

Computation of the crater size/frequency information (Appendix A) in this study was assisted by a software package written in house for the planetary science program by John Chappelow (PhD candidate, UAF). Using this software, the diameter of every crater in each of the images was measured and recorded, then binned and plotted according to widely used practices (Crater Analysis Techniques Working Group, 1979). Because the images are large, they were broken into image segments and counted as shown in Appendix B. The size-frequency distributions were examined individually for evidence of geological processes and compared to each other to look for variations and similarities. In order to make a comparison of the cratering record in areas of differing hematite concentration, the data was combined to create an aggregated size-frequency distribution for the five images measured within the Opportunity landing ellipse, and another for the six images measured within the region of Meridiani that shows the strongest hematite concentration. Additionally, all data were combined to create one size-frequency distribution representing the entire region to enhance statistical significance and show regional effects on the small crater population.

4 *Results of Size-Frequency Distributions*

Table 2 shows the number of craters measured in each size bin in each image, as well as the total number of craters measured in each size bin for all the images. For a simple, unmodified production population, the smaller size diameter bins should contain larger numbers of craters than their larger counterparts. Turndowns found in the smaller diameter bins may indicate preferential removal of small craters by geologic processes or atmospheric filtering of projectiles, but most probably reflects resolution/identification effects; at a minimum, four pixels are needed to identify a crater rim. Table 3 shows the map scale of each pixel times four pixels needed to identify the minimum size crater discernable in each of the images, the largest of which is 14.66 m. In table 2, the turndown ceases at the 15.63 m bin and was therefore chosen as a minimum size cut-off for the size-frequency distributions. The minimum size crater identifiable for each image is well below this value.

The size-frequency distribution of each of the eleven images measured is shown in Figures 4a-4k. Each point is plotted in the center of the bin and represents the number of craters in that bin divided by the area of the image. Error bars reflect the counting errors, which are determined by the square root of the number of craters in the bin divided by the area of the image (equation 3). If there is only one crater measured in a particular bin, then the error bars go to zero:

$$\frac{1}{area} - \frac{\sqrt{1}}{area} = 0.$$

This is a problem on a log-log graph. They are therefore shown to approach zero making a very large error bar. This is seen in most of the graphs particularly at larger diameters where the bins are less likely to have more than one crater in that size range. Such error bars reflect the low statistical significance of these data points.

Figure 4a shows the size-frequency distribution of MOC-NA image e0101056. In the 15.6 m to 44.2 m range, there is a trend in the data that follows Hartmann's 10 My isochron. In the 44.2 m to 176.8 m range, the trend in the data follows Hartmann's 100 My isochron. Above 176.8, there is an unusual amount of large craters that lie close to the saturation line.

Figure 4b shows the size-frequency distribution of MOC-NA image m0001660. In the 15.6 m to 44.2 m range, there is a trend in the data that follows Hartmann's 10 My isochron. There is only one crater that occurs in the 500 m bin (Table 2), but because the image area is only 10.4 km^2 (Table 1) the point on the size-frequency distribution hits the saturation line.

Figure 4c shows the size-frequency distribution of MOC-NA image e0500801. In the 15.6 m to 62.5 m range, the trend in the data is slightly less than but almost parallels Hartmann's 100 My isochron. At diameters above the 62.5 m bin, the data is erratic.

Figure 4d shows the size-frequency distribution of MOC-NA image m0802647. In the 15.6 m to 31.2 m range, there is a trend in the data that follows but is slightly offset from Hartmann's 10 My isochron. In the 31.2 m to 62.5 m range,

the trend in the data is slightly offset from Hartmann's 100 My isochron. The image area is only 6.28 km^2 (Table 1), which explains the lack of large craters.

Figure 4e shows the size-frequency distribution of MOC-NA image e0200373. In the 15.6 m to 250 m range, the trend in the data has a slope that is offset from but almost parallel to the saturation equilibrium line. In the 250 m to 707.1 m range, there is a trend in the data that follows Hartmann's 3 Gy isochron.

Figure 4f shows the size-frequency distribution of MOC-NA image m0704322. In the 15.6 m to 44.2 m range, there is a trend in the data that follows Hartmann's 10 My isochron. In the 62.5 m to 353.6 m range, the trend in the data is offset to but almost parallels the saturation equilibrium line. A break in the slope occurs at the 44.2 m bin.

Figure 4g shows the size-frequency distribution of MOC-NA image e0300624. In the 15.6 m to 44.2 m range, there is a trend in the data that follows Hartmann's 10 My isochron. In the 62.5 m to 353.6 m range, the trend in the data has a slope that lies fairly close to and is shallower than the saturation equilibrium line. The 250 m bin contains a higher than expected number of craters (12) (Table 2). A break in the slope occurs at the 44.2 m bin.

Figure 4h shows the size-frequency distribution of MOC-NA image e0301946. In the 15.6 m to 44.2 m range, there is a trend in the data that follows Hartmann's 10 My isochron. In the 62.5 m to 250 m range, the trend in the data is offset to but parallels the saturation equilibrium line. In the 353.6 m to 707.1 m range, there is a trend in the data that follows Hartmann's 3 Gy isochron. It is also

possible that from the 62.5 m to the 707.1 m bin, the trend in the data is offset to but almost parallels the saturation equilibrium line but there are no craters in the 250 m bin. A break in the slope occurs at the 44.2 m bin.

Figure 4i shows the size-frequency distribution of MOC-NA image e0201143. In the 15.6 m to 44.2 m range, there is a trend in the data that follows Hartmann's 10 My isochron. In the 62.5 m to 250 m range, the trend in the data is slightly offset to but almost parallels Hartmann's 100 My isochron. A break in the slope occurs at the 44.2 m bin.

Figure 4j shows the size-frequency distribution of MOC-NA image e0402072. In the 22.1 m to 62.5 m range, there is a trend in the data that follows Hartmann's 10 My isochron. In the 88.4 m to 353.6 m range, the trend in the data is offset to but parallels the saturation equilibrium line. A break in the slope occurs at the 62.5 m bin.

Figure 4k shows the size-frequency distribution of MOC-NA image e0503058. In the 15.6 m to 44.2 m range, there is a trend in the data that follows Hartmann's 10 My isochron. In the 62.5 m to 353.6 m range, the trend in the data is offset to but parallels the saturation equilibrium line. A break in the slope occurs at the 44.2 m bin.

Figures 4f through 4k have remarkably similar size-frequency distributions and were therefore all re-plotted on one size-frequency distribution (Figure 5a). They all show a small diameter trend along the 10 My isochron up to approximately D=40 m, and then a second trend whose slope is shallower than the isochrons but roughly

paralleling the saturation equilibrium line, in the range 70 m < D < 200 m. Interestingly, Figures 4f through 4k all occur in the area of highest hematite concentration. Figure 5b shows Figures 4a through 4e all plotted on one size-frequency distribution. These are all of the images that occur in the landing ellipse area.

Table 2 shows the decline in the number of craters counted toward larger diameters is more gradual from the 62.5 m bin to the 250 m bin in the highest hematite area than in the landing ellipse area. It is quite the opposite from the 31.2 m bin to the 44.2 m bin, with 62% more craters occurring in the landing ellipse area than the highest hematite area in the 31.2 m bin. This size range is interesting in the highest hematite area because there is a pronounced deficit of craters. Again, the smaller size diameter bins should have a greater amount of craters than their larger counterparts, but the data goes from N=392 (31.2 m bin) to N=264 (44.2 m bin) back up to N=309 (62.5 m bin) (Table 2).

This is seen graphically in the combined size-frequency distribution for the five images measured within the Opportunity landing ellipse (Figure 6) compared to the combined size-frequency distribution for the six images measured within the region of Meridiani that shows the strongest hematite concentration (Figure 7). Figure 8 is a plot of the totals from each area on the same graph, demonstrating the difference between the two and Table 4 highlights the characteristics of each region.

The landing ellipse area has fewer craters with diameters between 62.5 and 125 meters than the area of highest hematite concentration, and there is a small, but

significant dip in the 31.2 m to 44.2 m size range in the highest hematite size-frequency distribution. This dip in Figure 7 is absent in Figure 6. There is also a difference above the 500 meter bin. There are 10 craters greater than 500 meters in the images measured within the landing ellipse in an area of 219.5 km^2 (Figure 6), but only 2 craters greater than 500 meters in the images measured within the highest hematite concentration in an area almost double in size 409.5 km^2 (Figure 7). This is what accounts for the difference in slope at the larger craters between the two figures. The higher hematite concentration area has fewer large (500-1000 meter) craters.

The slope of the line for the size-frequency distribution of the combined total for all eleven images measured within Meridiani (Figure 9) roughly parallels the saturation equilibrium line, with a slight increase towards the larger (500-1000 meter) diameter craters due to the lack of the craters in this size range in Figure 7 as explained in the previous paragraph. The small but significant dip in the 31.2 m to 44.2 m size range can be seen, although less pronounced than in Figure 7.

5 Discussion

5.1 Comparison with theoretical models

The size-frequency distributions for all of the images of the highest hematite region (Figures 4f-k, Figure 5a) are strikingly similar, strongly indicating that the imaged areas have been shaped by the same geologic processes for at least 3 billion years (Figure 7). In chapter 8 of Basaltic Volcanism on the Terrestrial Planets, the Basaltic Volcanism Study Project (1981) has an extensive review on the history and method of crater counting. Figure 10 shows the graphical representation of the mathematical models of the variation that can occur on size-frequency distributions due to various geological events that have taken place on a given surface. Figure 10a shows the size-frequency distribution reflecting a stable surface with no geologic activity. Here the time-integrated effects of impact cratering have produced a "production population" with a slope, b=-3.82. A turndown at small diameters may reveal the effects of atmospheric shielding or may be due to the inability to identity and measure craters at the limits of image resolution (Figure 10b). Incorporation of secondary or endogenic craters may result in a slight steepening of the size-frequency distribution as shown in Figure 10c.

If a lava flow or ejecta blanket suddenly removes all craters by blanketing all features below a critical diameter, D_c, but leaving the bigger crater's rims still intact, the resulting size-frequency distribution would resemble Figure 10d. Continued cratering after the blanketing event would result in a bump left in the size-frequency distribution (Figure 10e). Figure 10f shows the result of repeated episodes of this

kind of crater removal with lava flows/ejecta blankets of varying depths. The slope has some decrease due to preferential removal of small craters.

A constant, slow deposition of material that uniformly rains on the surface would produce a slope of b+1 in the size-frequency distribution, in which the time to completely infill a crater is proportional to the diameter as shown in Figure 10g; steady erosion over time would produce the same effect. This effect obliterates small craters rapidly and larger craters slowly or not at all depending on the length of the episode. If this constant, slow deposition/erosion of material were to stop and cratering continue, the size-frequency distribution would look like Figure 10h.

The size-frequency distribution of the combined total for all eleven images measured within Meridiani (Figure 9) roughly parallels the saturation equilibrium line for all of the crater diameters that I measured, with a slight increase towards the larger (500-1000 meter) diameters. Figure 9 is not consistent with any of the theoretical examples shown in Figure 10. The closest size-frequency distribution that this area may resemble is the left half of Figure 10g, suggesting that crater obliteration processes have dominated the Meridiani region. However, the slope is greater than the given b+1 in Figure 10g. Given the assumption that a Hartmann isochron is a production function with slope b=-3.82 (Equation 1), the difference from the calculated slope in Figure 9 of -1.77 and the production function is 2.05, giving this size-frequency distribution a slope of b+2. Figure 10g corresponds to a constant, slow deposition of material; a process which obliterates smaller, shallower craters more rapidly than larger ones and craters above a certain depth not at all if there has

not been time for the oldest craters to be filled in, theoretically resulting in the shallower b+1 slope (Basaltic Volcanism Study Project, 1981).

The b+1 slope results from the assumption that the time it takes to infill a crater depends solely on its diameter (Öpik, 1966). This is equivalent to slow, steady infilling due to dust settling or pelagic sedimentation. Processes that don't follow this assumption may produce size-frequency distributions with very different slopes. This conclusion is independent of whether the obliteration process in question is an infilling process (Chapman and Jones, 1977) or an erosion process (Öpik, 1966). Either (or both) may be consistent with the shape of Figure 9.

The fact that Figure 9 is not consistent with any parts of Figure 10 suggests that the region of Meridiani sampled by my images is geologically complex. Sorting the images into two groups, six images that cross the highest hematite signature, and five that cross the Opportunity rover's landing ellipse, bears this out: the size-frequency distributions of cratering in the highest-hematite images (Figures 4f-k, Figure 7) are remarkably alike, and distinctly different than size-frequency distributions taken from the landing ellipse group (Figures 4a-e, Figure 6).

Figure 7, the combined size-frequency distribution for the six images within the region of Meridiani that shows the strongest hematite concentration most closely resembles a combination of a production population and an obliterative process (Figure 10a, Figure 10g). For diameters less than 44.2 m, Figure 7 reflects a production population of age 10 My, according to Hartmann's isochrons, indicating that little activity except cratering has occurred for the last 10 My similar to Figure

10a. The larger craters (>62.5 m) do not follow an isochron of a specific older age, but have shallower slopes of approximately b+2 that plot roughly parallel to the saturation equilibrium line, suggesting an obliteration process was occurring prior to 10 Mya. The bend in Figure 7 at about D = 300 m (the size-frequency distribution turns to follow the 3 Gy isochron at that point) suggests a production surface at 3 Gy, similar to Figure 10h. Note that contrary to the burial-metamorphism-exhumation theory for production of hematite (Hartmann, 2001a; Kelsey et al., 2000; Lane et al., 1999; and Gilmore and Tanaka, 2002), these results indicate a long period of obliteration in Meridiani from about 3 Gy until shortly before 10 My. The small but significant dip in the 31.2 m to 62.5 m size range resembles Figure 10e and could represent a relatively sudden geological event, such as volcanism, blanketing by ejecta, or severe aeolian activity.

The crater populations counted in the MOC-NA images that cross the Opportunity landing ellipse (Figures 4a-e) show considerably more variation. The images measured within the Opportunity landing ellipse have a size-frequency distribution with a slope close to b+2 across the entire range of diameters (Figure 6), suggesting that both cratering and some crater obliteration process were occurring similar as to that found in the highest hematite area. Otherwise, the size-frequency distributions for the two areas are quite different.

5.2 Comparison with Hartmann's crater counts

Hartmann (2004) has counted craters within MOC-NA image m0001661 in the Meridiani region (Figure 11a). The image lies northwest of the landing ellipse

and barely within the hematite signature (Figure 11a). His count is separated and plotted in two groups: "fossil craters" that apparently date back to very early Martian history and show a size distribution close to saturation equilibrium, and a population of small ($D < 250$ m), sharply defined, bowl shaped craters that have been accumulating only for the last ~ 10 My. He interprets this size-frequency distribution to indicate that

> the present surface (or top 80 m) has been exposed for $\leq\sim$ 10 My which in turn indicates an exhumation episode at around that time. The ancient surface itself, exposed by this exhumation, appears to date back to the first 20% of Martian history, and the hematite deposits in this area may relate to very early Noachian fluvial processes.

The data from Figure 9 of my study is plotted (shown with magenta circles) on top of Hartmann's size-frequency distribution of Meridiani for comparison (Figure 11a). Up to the 250 m bin, the data seems to average between Hartmann's two crater groups quite well (keep in mind that the axis is logarithmic), with the exception of the small but significant dip in the 31.2 m to 44.2 m size range representing a deficiency of craters in this size range shown in Figure 11a as feature A. Hartmann's size-frequency distribution does not exhibit this dip, however this may be a result of comparing an area of 629 km^2 to an area approximately 32 km^2. Also, MOC NA image m0001661 occurs near the landing ellipse area and as seen in Figure 6 the small but significant dip does not show in the size-frequency distribution within this region. Therefore, the data from Figure 6 was also plotted on top of Hartmann's

counts of Meridiani (shown with blue circles). The variation seen at feature A is reduced but is still significantly different than Hartmann's results. Above the 500 m bin the data is significantly different. Hartmann's graph has a data point above 2 km and data points between 16 km and 44 km. Since the width of the image Hartmann measured is 1.46 km, other larger images must have been used to get these data points but not cited. This data greatly affects the crater population above about 500 m.

Hartmann's interpretation of the data corresponds well with my findings for the highest-hematite area in that (1) the small crater population indicates a surface age of 10 My, (2) a geologically sudden crater obliteration event occurred about 10 My ago, and (3) the large ($D > 250$ m) crater population reflects a large-crater retention age of ~3 Gy. However, Hartmann does not explain his exhumation episode, how he came up with the top 80 m as defining the surface or why he thinks the deposits in this area relate to very early Noachian fluvial processes. He also does not explain the deviations in the slope of his data from that of the isochrons.

In order to get an idea of how this area's cratering record compares with that of other areas on Mars, the results from Figure 9 were plotted on top of various size-frequency distributions prepared by Hartmann (2004). The first area is heavily cratered terrain on the floor of the large crater Schiaparelli (shown with solid symbols), which in turn is situated in one of the most heavily cratered Martian terrains, south Arabia Terra (Figure 11b). The heavy, bent solid line is a predicted steady state line for a crater population that is being infilled at a net, average deposition rate of around 10^{-6} m/year (Hartmann, 2004). My data plots on top of all

data points within the error bars from 42.5 m up to 707.1 m thus showing that this area as well as Meridiani has experienced a long period of crater erosion. However, the data sets do not agree at smaller diameters. Therefore, this area has probably not experienced the same sort of recent (< 10 My) history as Meridiani.

Hartmann's plot of the old moderately heavily cratered plains around Nirgal Vallis is shown in Figure 11c. Hartmann believes that craters act as potential wells that preferentially fill with windblown dust faster than the surroundings and has therefore drawn the solid curve in his size-frequency distribution to show how he believes a net infill rate of about 10^{-6} m/year (Hartmann, 2004) would affect the crater population. My data points fall remarkably parallel to his data points and match at D>500 m. This suggests that these two areas may have a similar history in that they both have evidence of crater erosion over a period of time.

Figure 11d shows Hartmann's crater counts at the Pathfinder landing site at the mouth of Ares Vallis, a large water or debris outflow channel (Tanaka, 1998). This site's crater population suggests a model age for the surface layers of about 0.5 to 2 Gy, based on craters from D=~200 m to ~8 km (Hartmann, 2004). My data points overlie Hartmann's from 176.8 m up. However, the results don't match for smaller diameters; Hartmann's results indicate that the site has been static for about the past 1 Gy, as suggested above, while in contrast my results show recent geologic activity in Meridiani.

Another landing site, Viking 1, is shown in Figure 11e. It is situated in Chryse Planitia, which is downstream from several outflow channels, including Ares

Vallis. At smaller sizes (D<~3 km), the data appear to fit the production function shape quite well with a model age of about 1-2 Gy, with the usual factor of perhaps 2 or 3 Gy uncertainty in absolute age (Hartmann, 2004). The bent, solid line is a theoretical steady state assuming steady crater infill and obliteration; it fits old upland surfaces on Mars, but the Viking 1 data fall below it at D=250m to 32km, and fit better to the isochrons (Hartmann, 2004). Hartmann's interpretation is that the Viking 1 site is young enough to preserve the production function at D>250m. My data fall on top of Hartmann's data from 250 m up to 707.1 m, but below $D = 250$ m Hartmann's size-frequency distribution appears to be saturated, indicating a lack of recent geologic activity very similar to the Pathfinder landing site (Figure 11d).

Figure 11f and 11g show Hartmann's counts of Olympus Mons, the first counting older flows averaging over the older background surface of Olympus Mons, using Mariner and Viking data and an average of several MGS and THEMIS frames, and the second dramatic examples of younger flows. The data for Figure 11f, averaging over much of the slopes and summit, fit an isochron giving a characteristic model age of about 200 to 800 Ma and the data for Figure 11g, while giving poorer statistics because of the sparse cratering, gives a model age of about 10 to 200 My (Hartmann, 2004). My data fit the older flows from 62.5 m up to 353.6 m and almost fit the data from 15.6 m to 31.2 m on the younger flows.

A very young area is shown in Figure 11h, which crosses a strip of the floor of the summit caldera of the very young Tharsis volcano, Arsia Mons. At the upper left, the curve runs into the solid saturation equilibrium line at D ~ 60 m because the

caldera lavas are so young that no substantial obliterative losses have occurred even for craters as small as 60 m, or depths as shallow as about 10 m (Hartmann, 2004). The isochrons suggest that the average surface age of the last major flows covering the caldera is around 100-300 My old, while the characteristic mean surface age of flows constituting the larger Arsia Mons structure is around 200-1000 My (Hartmann, 2004). My data roughly matches Hartmann's points from 125 m to 500 m, though my points tend to lie slightly above Hartmann's. My data does not match Arsia Mons below $D = 125$ m because of Arsia's lack of obliteration processes for 100-300 My.

The last two examples, Figures 11i and 11j, both have size-frequency distributions that only fit my data from 31.2 m to 44.2 m. The first of these is Amazonis Planitia. The older lava flows of Amazonis Planitia appear to fit the isochrons well giving a model age of about 100 My to 1000 My, interpreted as the true age of the flows, and the younger flows give a model age of about 9 My to 90 My for the youngest flows (Hartmann, 2004). The second is Marte Vallis, a geologically young outflow channel. Crater counts in and around various parts of Marte Vallis fit an isochron with model age around 30-300 My, which is interpreted by Hartmann as the age of the last major water flow in the system possibly being produced by melting of massive ground ice during the emplacement of the very recent surrounding lavas, which also date from the last few hundred My (Hartmann, 2004).

In Figures 11b through 11h, I have compared various martian surfaces, including an old heavily cratered terrain, a moderately heavily cratered plains, an

outflow channel and outflow plain, and several volcanic terrains to the Meridiani area. None of the size-frequency distributions from the above examples fit my data exactly from end to end, except possibly the Nirgal Vallis plains (Figure 11c). Evidence from the cratering record shows that Meridiani does not appear to correspond to any of these terrains, or at least it doesn't have the same history as any of them. However, Figures 11a-d, f, and h all exhibit a b+2 slope in the midsize crater range, not all that dissimilar from those in the Meridiani study area. Therefore, I believe that obliterative processes are common on Mars in that they are reflected in the size-frequency distribution of many various regions. Several of these terrains' size-frequency distributions show little evidence of recent activity. It is unique that the Meridiani region is experiencing a geologically recent resumption of a production function.

5.3 Constraints upon the nature of hematite in Meridiani

Another comparison was made closer to the hematite signature than that compared in Figures 11b-h with an image approximately 350 km from the eastern boundary of the hematite signature within the Meridiani region. In Figure 12, a size-frequency distribution constructed for image m1801300 located in northeast Meridiani at 0.14°S, 5.92°E was compared to the combined results of the highest hematite area (Figure 7). Every data point, with the exception of the 500 m bin, falls equidistantly below the corresponding point in the highest-hematite size-frequency distribution making the two size-frequency distributions essentially parallel. Even though there is no record of hematite in this image's area, their histories as

determined by the size-frequency distributions are very similar suggesting that the geologic history of the area with the hematite concentration is not unusual. The integrated affect of surface activity of Meridiani is no different, which therefore cannot explain the presence of the hematite. The hematite is a unique feature, yet the crater population in the area that it occurs is not unique compared to areas just outside the hematite signature and elsewhere on Mars (e.g. Nirgal Vallis).

One of the theories of the origin of the hematite is that it was deposited under a long-standing lake of water that once covered the hematite area. From my results it appears that over the last 3 billion years, this area has sustained a modest regime that has no discrete inundation required by a lake or required for shielding but only modest erosion of a pre-existing surface. Otherwise the crater population in the hematite region would show a record of it and not resemble the size-frequency distributions of other areas on Mars.

Three possible speculations for the nature of the hematite are as follows: 1) the hematite formed during early Martian history prior to 3 Gy, 2) unusual precursor materials formed at that time and the hematite developed through subsurface aqueous alteration 3) the hematite is being concentrated as lag deposits by aeolian winnowing that has occurred relatively recently.

5.4 Nature of recent activity in the region: evidence of abundant aeolian activity, an example from MOC-NA image m0704322

The size-frequency distribution for MOC-NA image m0704322 is particularly interesting as it features two different changes of slope (Figure 13, Table 2). Visual

inspection of image m0704322 (Figure 14) combined with analysis of crater size-frequency information reveals the presence of three distinct geological units represented by three populations of impact craters: an ancient, underlying unit (Unit 0) consisting of mostly buried stealth craters, a bright (high-albedo) cratered unit containing a relatively high density of small (5-50 m) impact craters (Unit 1), and a dark dune-enriched unit (Unit 2) that is encroaching upon the bright cratered unit (Chappelow et al., 2002)(Figure 15).

Separate size-frequency distributions were prepared for the two surface units present in image m0704322 on top of Hartmann's isochrons (Figure 16). After they are separated, differences in the size-frequency distributions clearly support the presence of these three distinct units and allow a more detailed assessment of the history of this region. All three units are dominated by aeolian activity. The geologic history derived from this study is as follows.

Unit 0 (mostly buried). This unit is characterized by buried 'stealth' craters with diameters from 30 m up to about 80 m, and larger, nearly buried heavily degraded craters up to ~150 m in diameter. The stealth craters are distributed ubiquitously throughout the image and are discernable, primarily by virtue of the low-albedo nature of the materials filling them. The larger of the craters of this population retain rim topography and interior relief, and without exception, show less degradation than their smaller counterparts. The larger members of this population exhibit well defined dune fields in their floors and dark wind streaks extending to the north from the crater rim.

The density of 'stealth' craters in the image suggests that Unit 0 is a very ancient surface, possibly extending to the time before the end of the Heavy Bombardment prior to 3.8 Gy ago. The imaged region lies ~5 km east of a 5-6 km impact crater and ~25 km northwest of a 40 km impact crater (Figure 17). As the proximal ejecta blanket of typical martian craters extends up to one crater diameter beyond the rim, it is likely that Unit 0 consists solely of impact debris and secondary craters from these larger craters. The ejecta blankets of all of these craters have been completely buried, providing further evidence that Unit 0 is an ancient surface. This burial is interpreted to indicate resurfacing of this primary ancient surface by a slow, steady state process such as continual deposition.

Unit 1 (bright cratered unit). This unit is confined primarily to the southern and eastern portion of the image, is a relatively high-albedo surface containing a relatively high density of small (5-50 m) impact craters, and exhibits little evidence of dunes.

The size-frequency distribution for Unit 1 roughly parallels the 10 My isochron which indicates a production population of craters. This suggests a recent resumption of a production population of craters after an obliterative process responsible for the slow resurfacing of this area abated, possibly as recently as a few million years ago. Little activity has occurred on the exposed surfaces of Unit 1 since that time.

Unit 2 (dark aeolian unit). This unit contains extensive dune fields over much of its surface and barchan dunes in the dune field in the northwest corner of the image

indicate a westerly prevailing wind (though the wind streaks on two large craters indicate a south-southeasterly wind). The orientations of these dune fields suggest encroachment onto Unit 1 by sediment migrating from the southwest. Several larger craters (up to >200 m in diameter) occur within Unit 2 but their morphologies indicate that they are inliers of Unit 0 protruding through the younger sedimentary cover comprising Unit 2. As previously noted, stealth craters (<80 m in diameter) appear to be nearly completely buried by Units 1 and 2. Assuming that the rim heights of these simple craters are approximately 4% of the rim diameter (Melosh, 1989), the thickness of Units 1 and 2 cannot greatly exceed ~3-4 m in places.

Unit 2's size-frequency distribution slope is slightly shallower than the saturation equilibrium line for D>~30 m. This indicates that Unit 2 has inherited some effects of the subjacent Unit 0, which is an ancient heavily cratered surface. The exceedingly shallow slope for Unit 2 at D>30 m indicates that Unit 0 has been strongly affected by a process that preferentially removed craters with small diameters. Both the slow steady aeolian process and the more recent aeolian activity from the west may be involved in this, especially in light of the preponderance of dunes on this Unit 2.

The size-frequency characteristics of small (12m<D<22m) craters on Unit 2 are approximately equivalent to the 5 My isochron of Hartmann. This information indicates a recent period of relative stability in the region (i.e. a reduction of the encroachment of aeolian material from the west), and suggests that the dune fields visible over large portions of Unit 2 may now be indurated. This could account for

the disparity between the migration direction of dunes and the SSE orientation of dark wind streaks that appear leeward of large craters.

The area covered by MOC image m0704322 in the northeast portion of the hematite-rich Meridiani region of Mars appears to represent an ancient ejecta blanket deposit (Unit 0) that has experienced continual but modest resurfacing by aeolian activity over the last few billion years (Unit 1). More recently, aeolian sediments (Unit 2) encroached upon Unit 1 from the west or southwest. The exposed portion of Unit 1 has remained stabilized since ~20 My and the small impact craters on Unit 2 indicate that its conspicuous dune fields may represent aeolian activity that dates back to ~ 5 My; thus these prominent dunes may be fossilized. More recent, modest aeolian activity is evidenced by well-developed north-northwest oriented wind streaks on the leeward side of the larger impact craters in the image.

5.5 Permissible depth of erosion in Meridiani

Because of the parabolic cross section of a simple crater (Melosh, 1989), erosion will decrease its apparent diameter as shown in Figure 18. If a crater of depth, d_i, over a period of time has undergone an amount of erosion, de, its residual depth would be d_f, where subscript i denotes the initial condition of the crater and subscript f denotes the final or current condition of the crater (Figure 18).

Laboratory and field studies have shown that the depth of the original simple crater is one-fifth its diameter or two-fifths its radius (Melosh, 1989):

$$d_i = \tfrac{1}{5} D_i = \tfrac{2}{5} R_i \qquad (5)$$

Most simple (bowl-shaped) craters have parabolic cross sections (e.g. Chappelow and

Sharpton, 2002) so that the crater profile is described by the equation;

$$z = \alpha r^2 \tag{6}$$

where $\alpha = \frac{4}{5D_i} = \frac{2}{5R_i}$ to satisfy equation 5 at the rim of the crater. So, for the original crater:

$$d_i = \alpha R_i^{\,2}$$

If this crater is eroded down so that its final depth is now d_f, equation 6 still describes its shape, but its depth and radius are now smaller:

$$d_f = \alpha R_f^{\,2}$$

The amount of erosion, *de* is just the difference (d_i - d_f):

$$d_i - d_f = \alpha\left(R_i^{\,2} - R_f^{\,2}\right)$$

$$d_i - d_f = \frac{2}{5R_i}\left(R_i^{\,2} - R_f^{\,2}\right) \tag{7}$$

$$de = \frac{2R_i}{5}\left(1 - \frac{R_f^{\,2}}{R_i^{\,2}}\right) = \frac{D_i}{5}\left(1 - \frac{D_f^{\,2}}{D_i^{\,2}}\right)$$

Equation 7 can been employed on the data points that fall between the 10 My production function at the smaller diameters and the 3 Gy production at the larger diameters in the size-frequency distribution of Figure 7 (44.2 to 250 m range). Points 1 through 5 are shown by green ellipses, in Figure 19, that coincide with the 44.2 to 250 m range. The original diameter, D_i, can be found by calculation of where it would fall on the nearest production function. Each of these points is traced to the 3 Gy isochron, an assumed point where erosion has not yet occurred. An example is

shown with point three. First the number of craters in the bin per unit area (N) is found (orange arrow) and then this number is used in equation 2, Hartmann's isochron equation, to find at what diameter this number of craters per unit area would occur on a 3 Gy old surface (blue arrow). The diameter is used in equation (7) to derive the depth of erosion. Applying the depth of erosion equation (7) to this area in the Meridiani region shows that the average amount of erosion that is consistent with the size-frequency distribution is 23 m (Table 5). The diameter at which the size-frequency distribution starts to follow the 3 Gy isochron is 250 m. If the 3 Gy isochron is indeed a production function, the constraint upon the maximum erosion in the region is one-fifth the depth of the 250 m bin or 50 m. However, the average erosion of 23 m is more plausible. This is clearly not thick enough of a surface layer to facilitate burial metamorphism of hematite as suggested by Lane et al. (2002).

6 Conclusion

Similarities of the size-frequency distributions between the regions of varying hematite concentration as well as between Meridiani and other regions of Mars (e. g. Nirgal Vallis, Arabia Terra) indicate that, along with impact cratering, the same basic obliteration process has acted on all these areas over long portions of Martian history ($\geq$ 3 Gy). The slope of these size-frequency distributions is considerably shallower than predicted by the Opik (1966) model for infilling of craters by dust; however this model did not account for lateral movement, near-surface shear, and erosional activity associated with aeolian activity. Abundant wind streaks and dunes within the Meridiani region such as those seen in example MOC-NA image m0704322 demonstrate the importance of these aeolian processes. Perhaps the aeolian processes make craters harder to completely remove than the Opik model proposes giving rise to a shallower slope.

Of the size-frequency distributions within the study area, the highest hematite area is the only one to show a production slope in the smaller crater population, which indicates little activity except cratering has occurred there for the last 10 My (Figure 7). Also shown in this size-frequency distribution is an erosional event that occurred approximately 10 to 100 My ago revealed by the small but significant dip in the 31.2 m to 62.5 m size range. Applying the depth of erosion equation (7) to this erosional event with the diameters between the assumed production functions at 10 My and 3 Gy shows that the average amount of erosion consistent with the size-frequency distribution is 23 meters (Figure 19, Table 5). Consequently, in the last 3 Gy there

has been an inadequate amount of burial to induce metamorphism in the Meridiani hematite as previously proposed by Lane et al. (2002).

There is no evidence of an extensive period of flooding or standing body of water that would have resulted in removal of craters or a shielding effect influencing the cratering record in the last 3 Gy. Consequently it is unlikely that the hematite deposits within Meridiani represent lake deposits unless, of course, the lake pre-dates the era of Martian history documented by the small crater population. The hematite or a precursor to hematite would have had to be emplaced very early in the history of Mars.

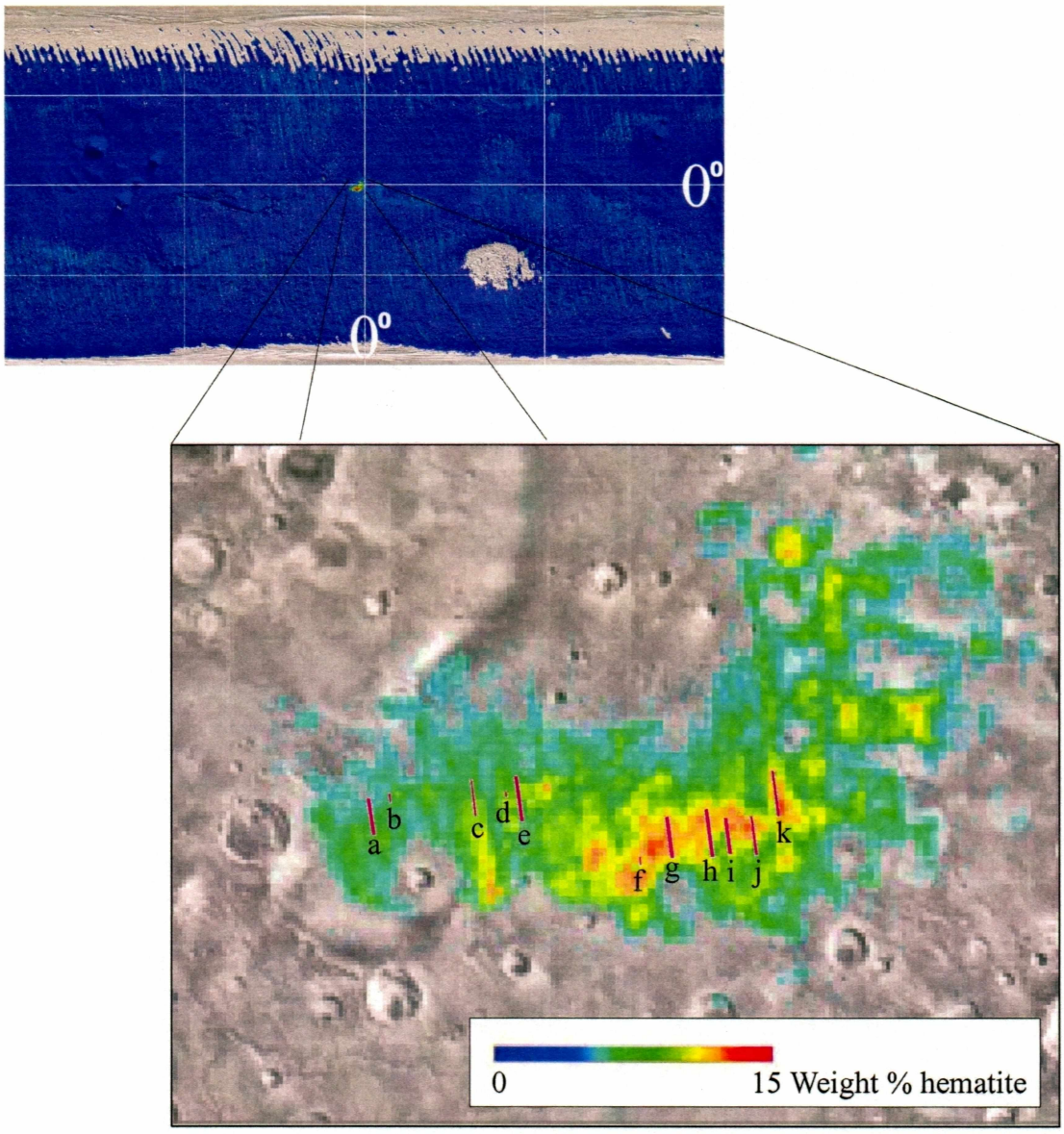

Figure 1: Mineral map of the distribution of hematite on the planet Mars. Both images are adapted from Christensen et al. (2000). The purple indicates no hematite thus showing the uniqueness of the deposit located near 0°, 0°. The inset is zoomed into this unique hematite signature within the Meridiani region. Darker red is higher hematite concentration (~15 weight percent). The footprint of a series of images measured in this study are shown by pink boxes. From left to right, they are a) e0101056, b) m0001660, c) e0500801, d) m0802647, e) e0200373, f) m0704322, g) e0300624, h) e0301946, i) e0201143, j) e0402072, and k) e0503058. Images a through e are within the landing ellipse for Mars Exploration Rover Opportunity and images f through k occur within the area of highest hematite concentration. Image information can be found in Table 1 and corresponding size-frequency distributions can be found in Figures 4a-4k.

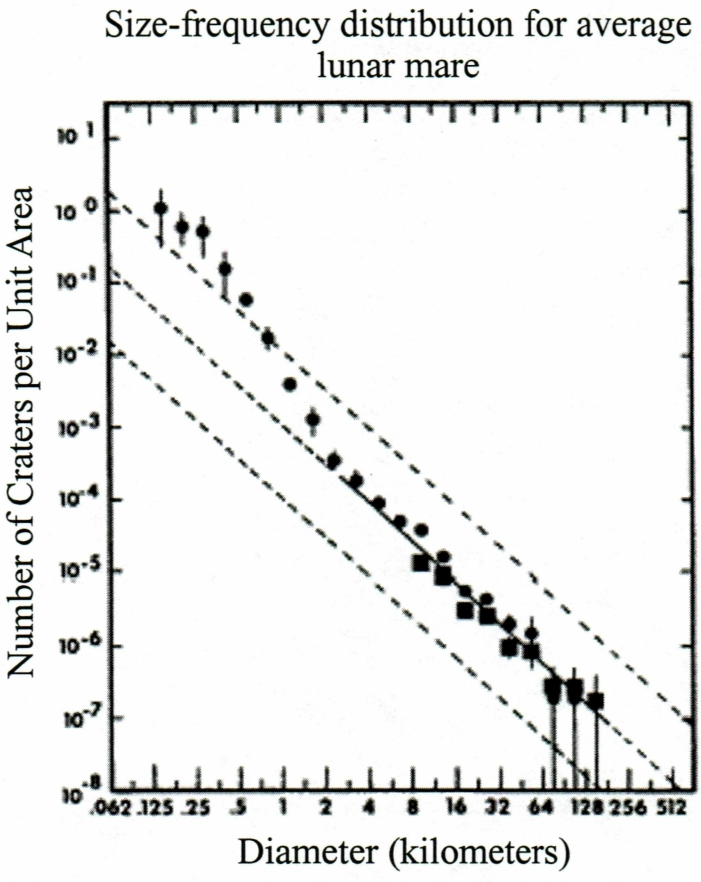

Figure 2: An example size-frequency distribution of the average lunar mare. This was adapted from the Basaltic Volcanism Study Project (1981). The solid line is a main reference curve of the fit to counts averaged over lunar maria. This solid line is extrapolated to smaller diameters shown by the middle dashed line. The upper and lower dashed lines are 10 times and 0.1 times the lunar mare reference line, respectively, to serve as references in estimating relative crater densities in different planetary provinces.

LEVELS OF ISIS MGS/MOC PROCESSING

Image Selection and Data Acquistion

- User identifies raw images to process.
- Use the image catalog system to find images in area of interest.
- Acquire image data from Planetary Data System Imaging Node via CD-ROM or Internet access.

Level 0 - Prepare raw image data for ISIS processing

- Read raw image file and convert to ISIS format.
- If raw image is compressed, decompress the image.
- Obtain SPICE information(navigation and pointing data) for raw image and place in ISIS labels.

Level 1 - Radiometric Correction

- Remove image artifacts (salt and pepper blemishes and coherent noise).
- Remove camera shading (correct for the gain and dark-current variations across field of view).
- Convert pixel values to radiometric units (radiance or "I/F").

Level 2 - Geometric Processing

- Perform geometric transformation (correct optical distortion and transform image from spacecraft camera orientation to the Sinusoidal Equal-Area projection).

Level 3 - Photometric Correction

- Adjust scene brightness by applying photometric normalization.
- Scene brightness of individual images balanced to minimize brightness differences along image boundaries.

Figure 3: Flow chart of image processing steps used in ISIS (Integrated Software for Imagers and Spectrometers). These processing steps are automated and used for various planetary image data sets. Adapted from http://isis.astrogeology.usgs.gov/Isis2/isis-bin/intro_digi_mosaic.cgi.

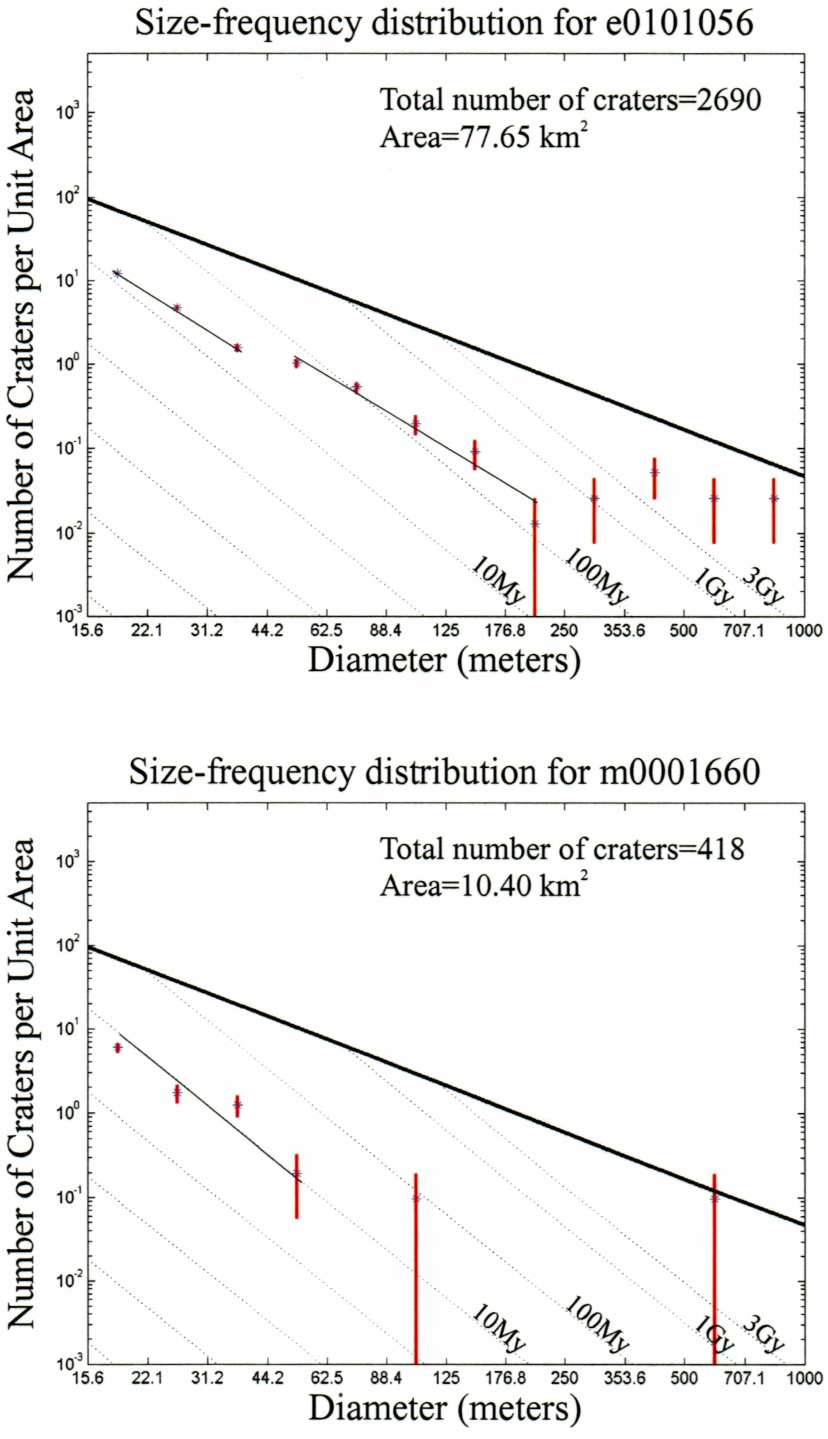

Figure 4a (top): Size-frequency distribution for e0101056. Figure 4b (bottom): Size-frequency distribution for m0001660. The solid line represents saturation equilibrium and the light dashed lines are isochrons of various ages (after Hartmann, 2002). The light solid line is the fit to the data. Error bars are shown in red. Corresponding image locations can be found in Figure 1.

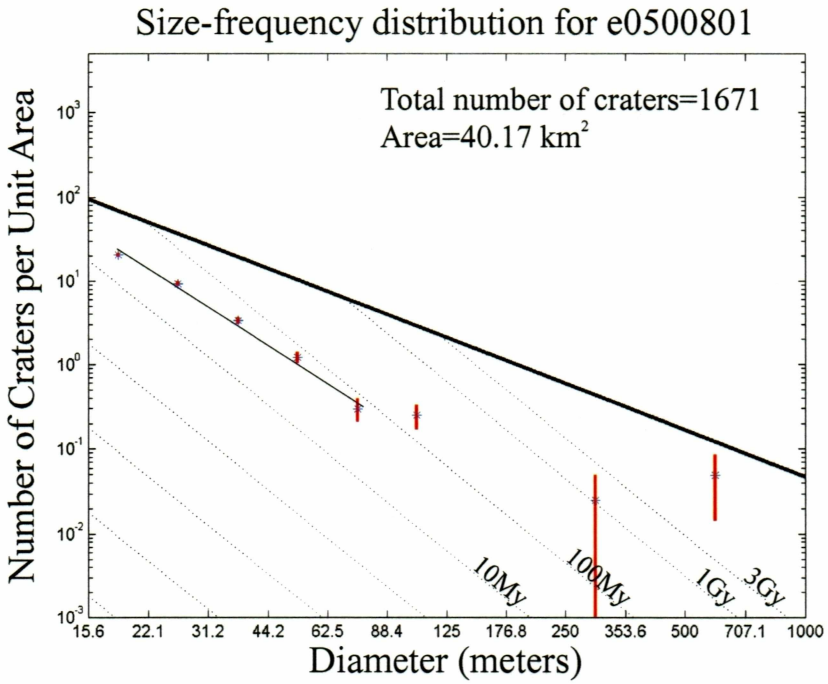

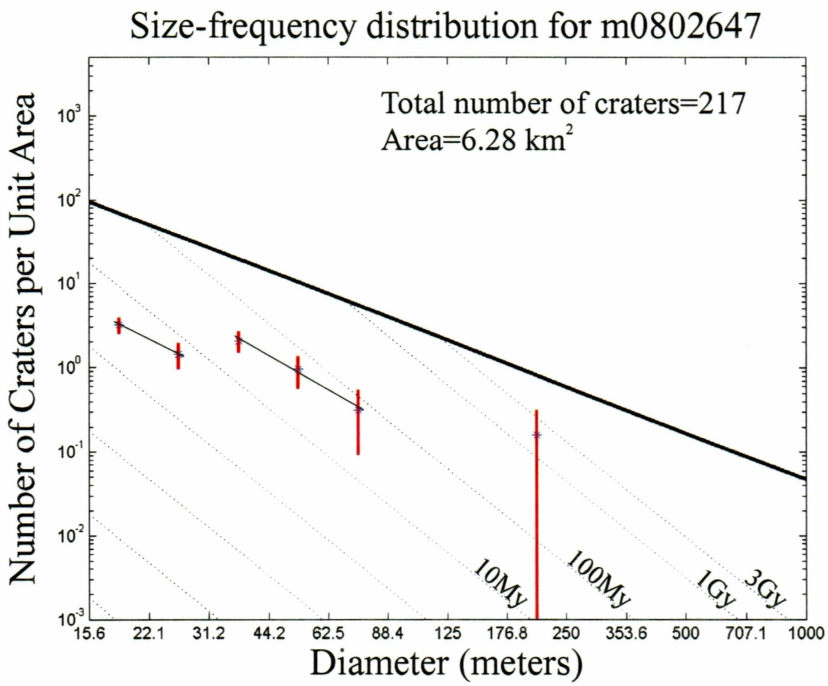

Figure 4c (top): Size-frequency distribution for e0500801. Figure 4d (bottom): Size-frequency distribution for m0802647. The solid line represents saturation equilibrium and the light dashed lines are isochrons of various ages (after Hartmann, 2002). The light solid line is the fit to the data. Error bars are shown in red. Corresponding image locations can be found in Figure 1.

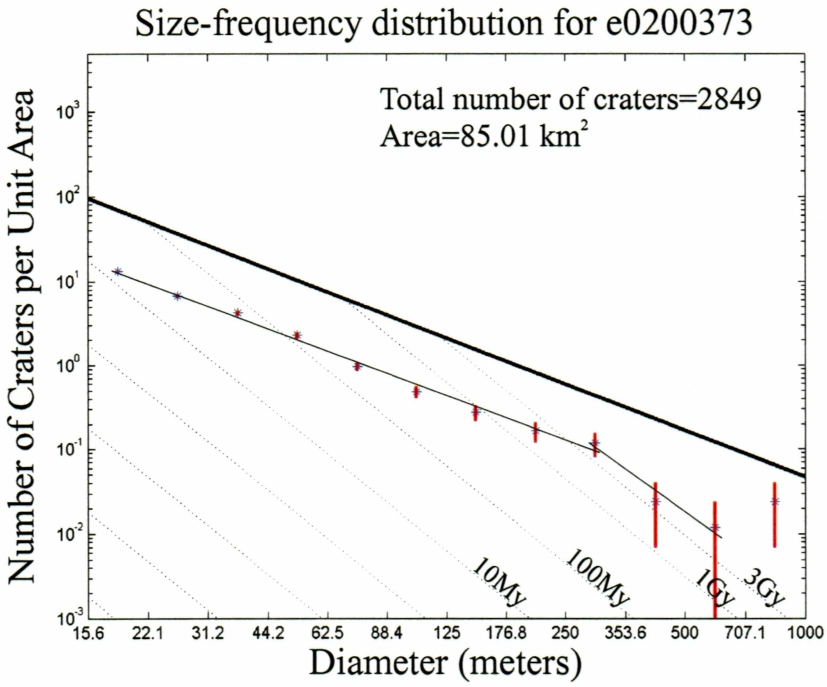

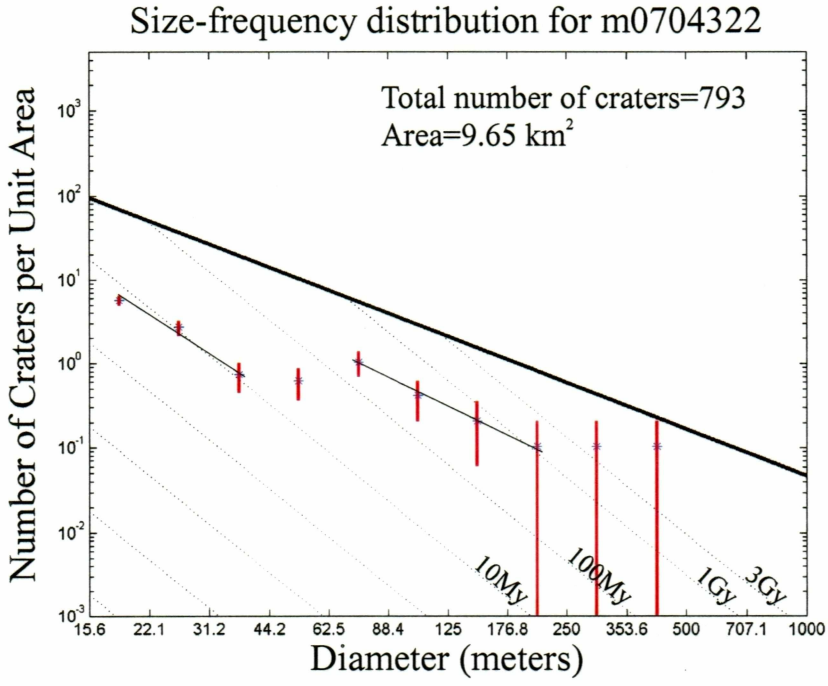

Figure 4e (top): Size-frequency distribution for e0200373. Figure 4f (bottom): Size-frequency distribution for m0704322. The solid line represents saturation equilibrium and the light dashed lines are isochrons of various ages (after Hartmann, 2002). The light solid line is the fit to the data. Error bars are shown in red. Corresponding image locations can be found in Figure 1.

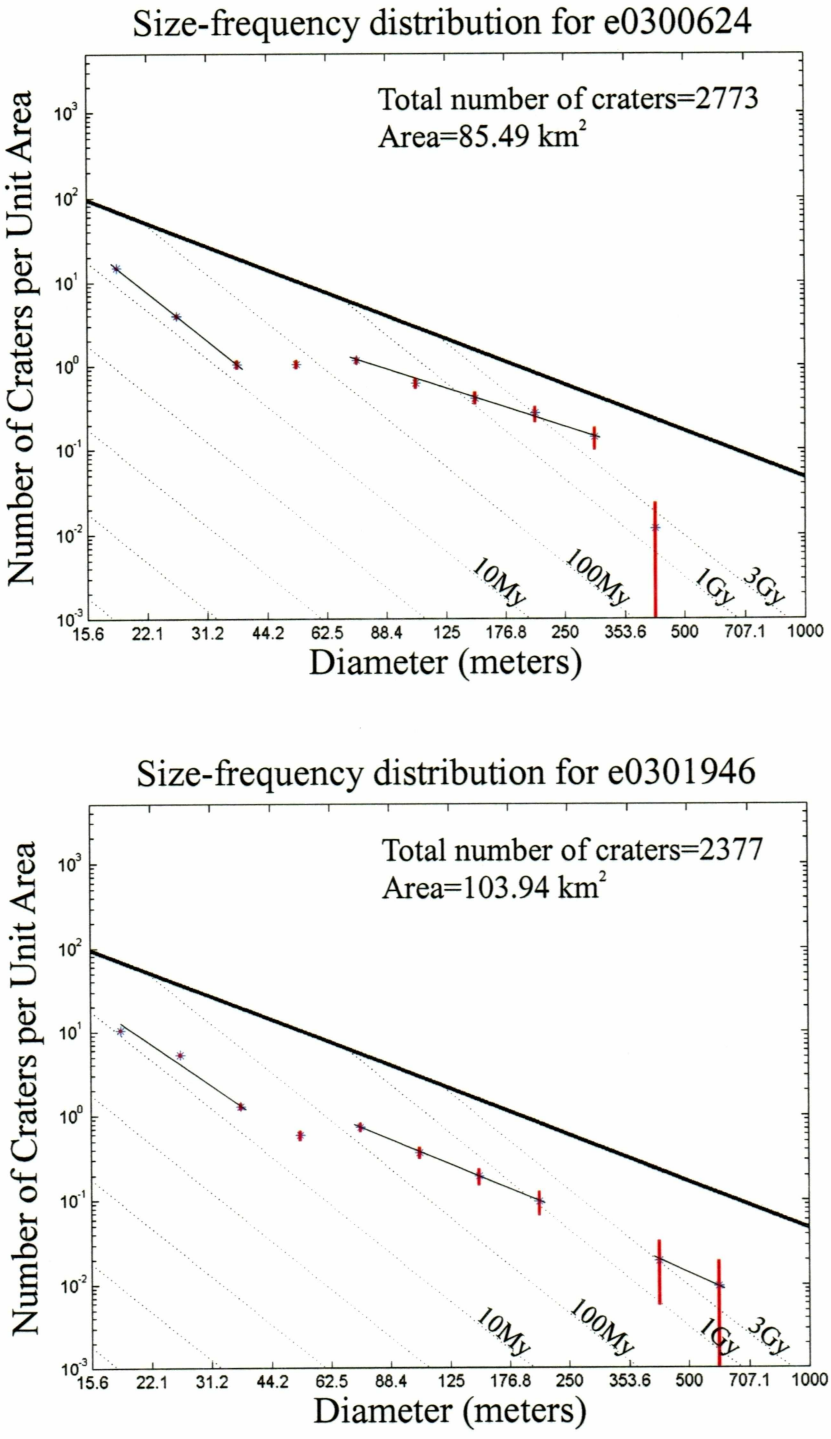

Figure 4g (top): Size-frequency distribution for e0300624. Figure 4h(bottom): Size-frequency distribution for e0301946. The solid line represents saturation equilibrium and the light dashed lines are isochrons of various ages (after Hartmann, 2002). The light solid line is the fit to the data. Error bars are shown in red. Corresponding image locations can be found in Figure 1.

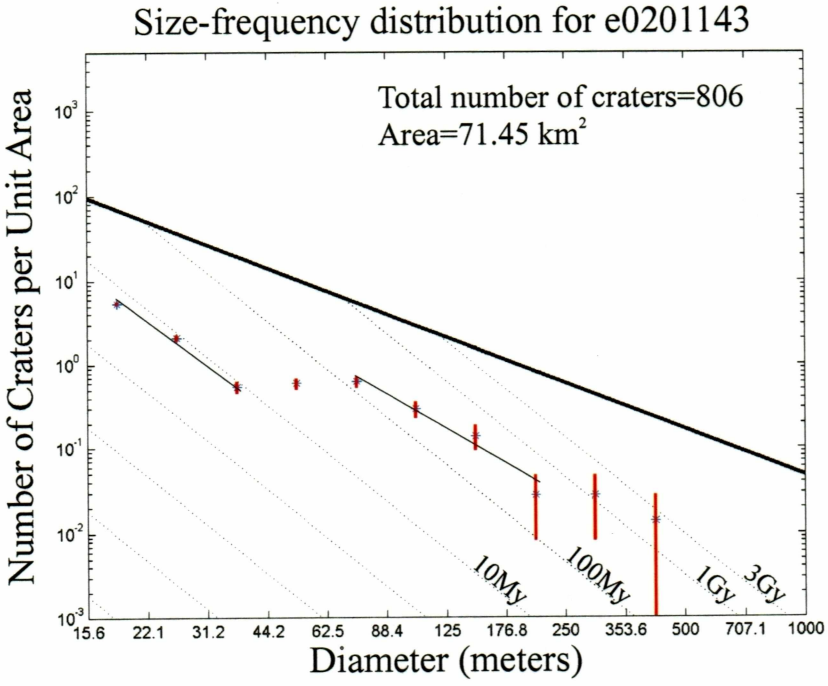

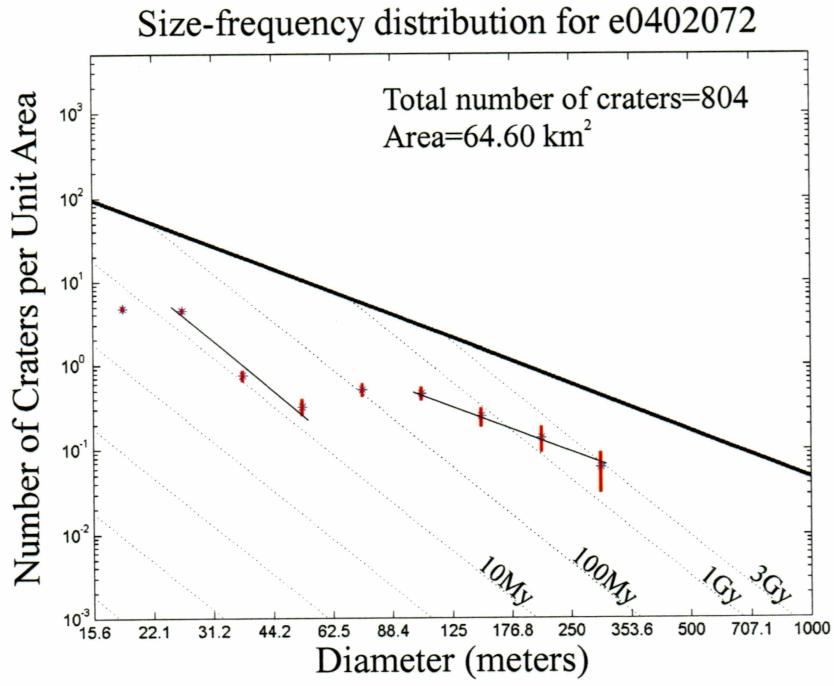

Figure 4i (top): Size-frequency distribution for e0201143. Figure 4j (bottom): Size-frequency distribution for e0402072. The solid line represents saturation equilibrium and the light dashed lines are isochrons of various ages (after Hartmann, 2002). The light solid line is the fit to the data. Error bars are shown in red. Corresponding image locations can be found in Figure 1.

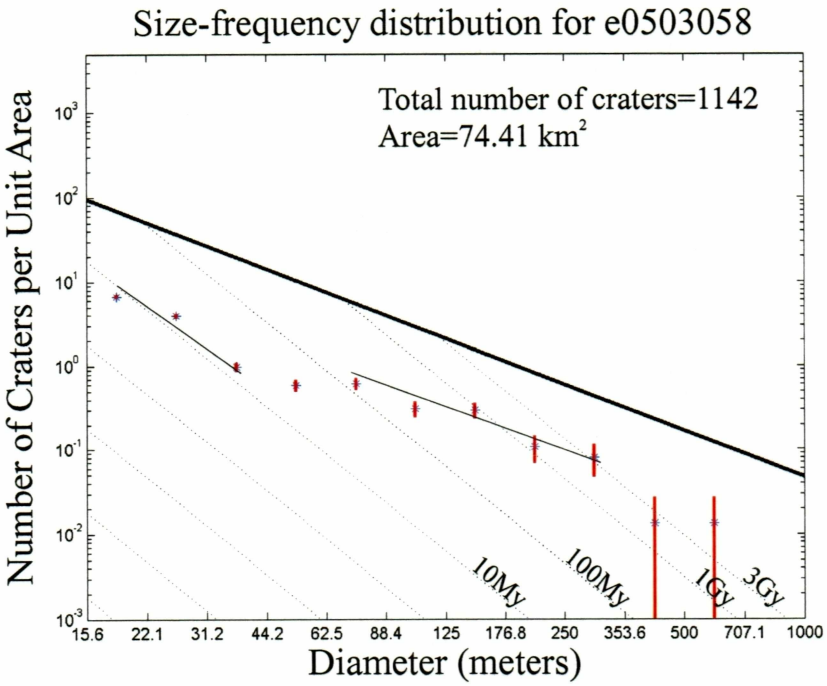

Figure 4k: Size-frequency distribution for e0503058. The solid line represents saturation equilibrium and the light dashed lines are isochrons of various ages (after Hartmann, 2002). The light solid line is the fit to the data. Error bars are shown in red. Corresponding image location can be found in Figure 1.

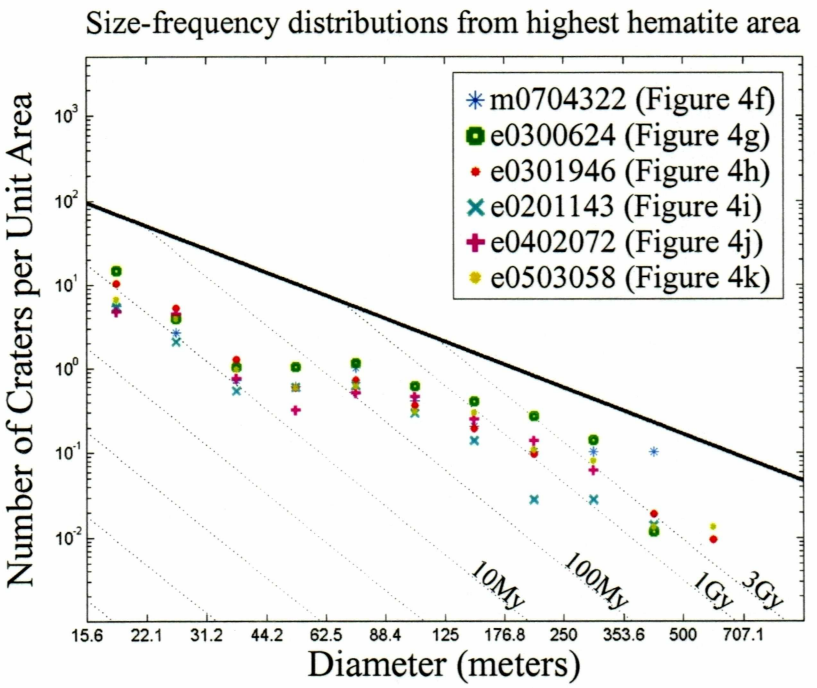

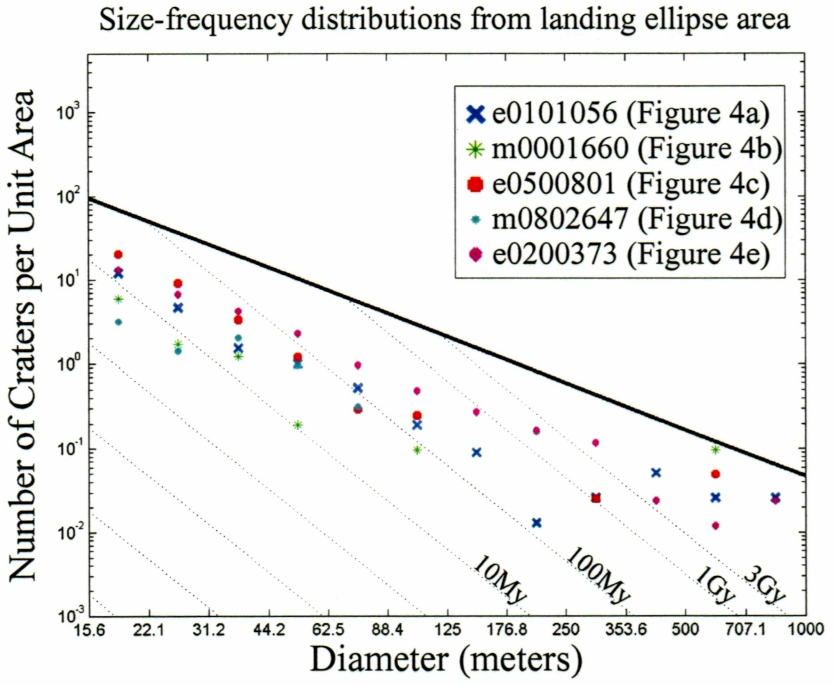

Figure 5a (top): Individual size-frequency distributions plotted on one graph of six images from the highest hematite area. Figure 5b (bottom): Individual size-frequency distributions plotted on one graph of five images from the landing ellipse area. The solid line represents saturation equilibrium and the light dashed lines are isochrons of various ages (after Hartmann, 2002). Error bars are omitted for clarity.

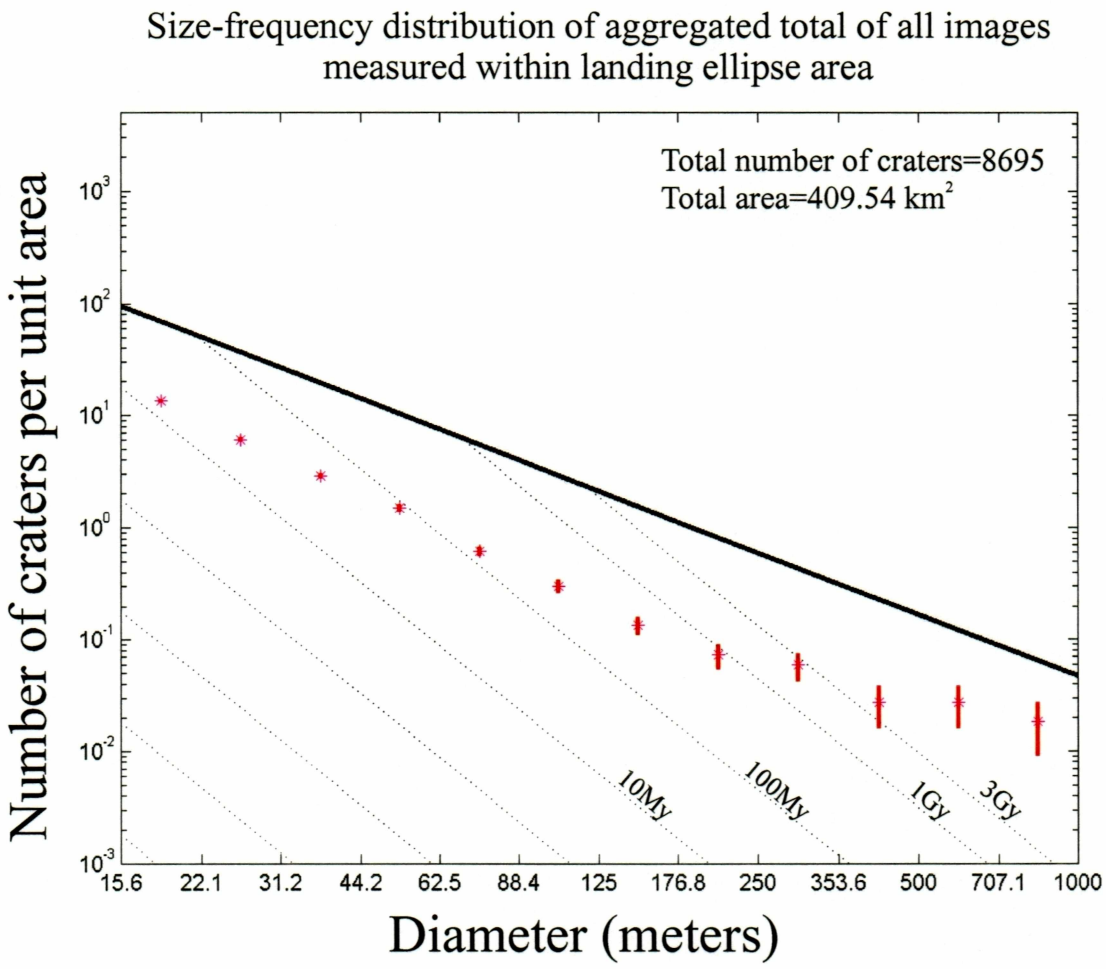

Figure 6: Size-frequency distribution for the aggregated total of the five images measured within the Opportunity landing ellipse. The solid line represents saturation equilibrium and the light dashed lines are isochrons of various ages (after Hartmann, 2002). Error bars are shown in red.

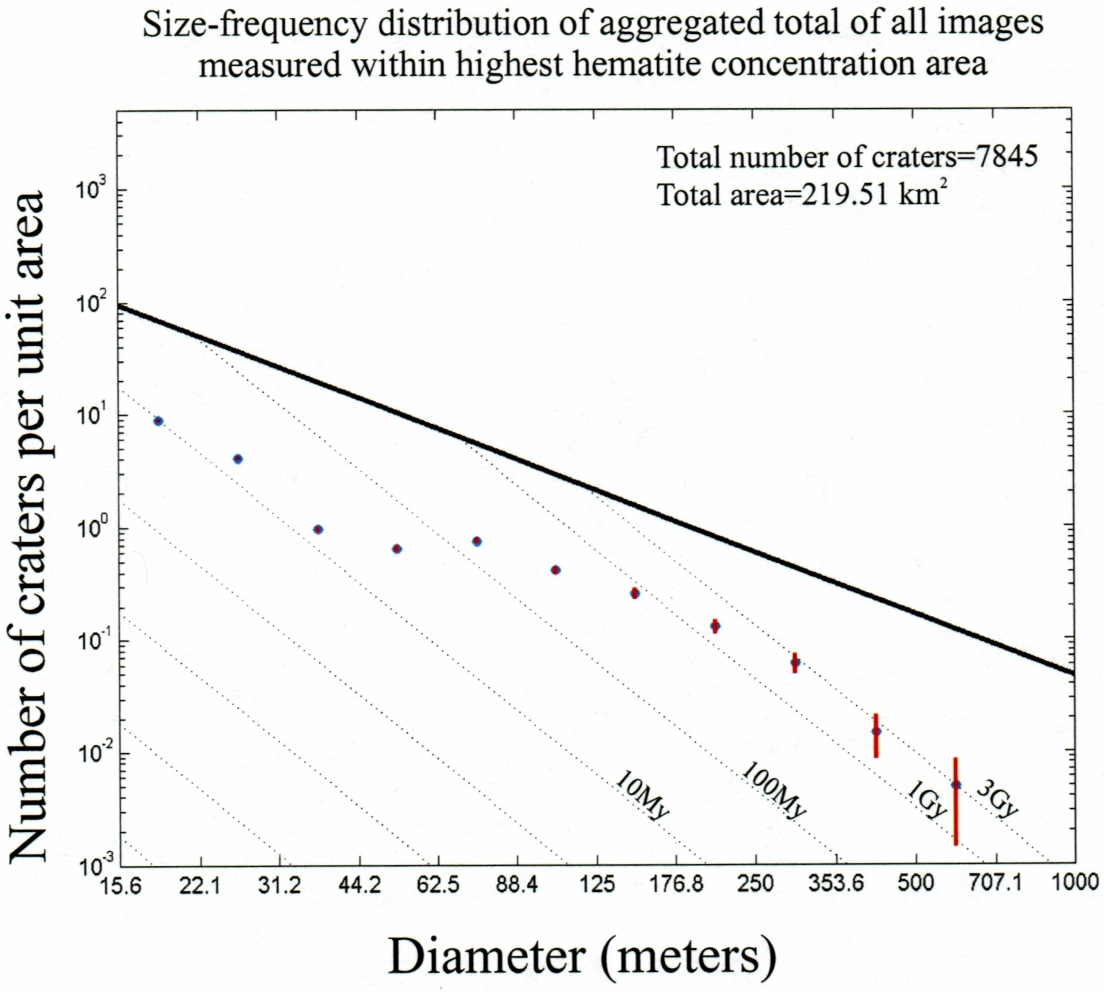

Figure 7: Size-frequency distribution for the aggregated total of the six images measured within the region of Meridiani that shows the strongest hematite concentration. The solid line represents saturation equilibrium and the light dashed lines are isochrons of various ages (after Hartmann, 2002). Error bars are shown in red.

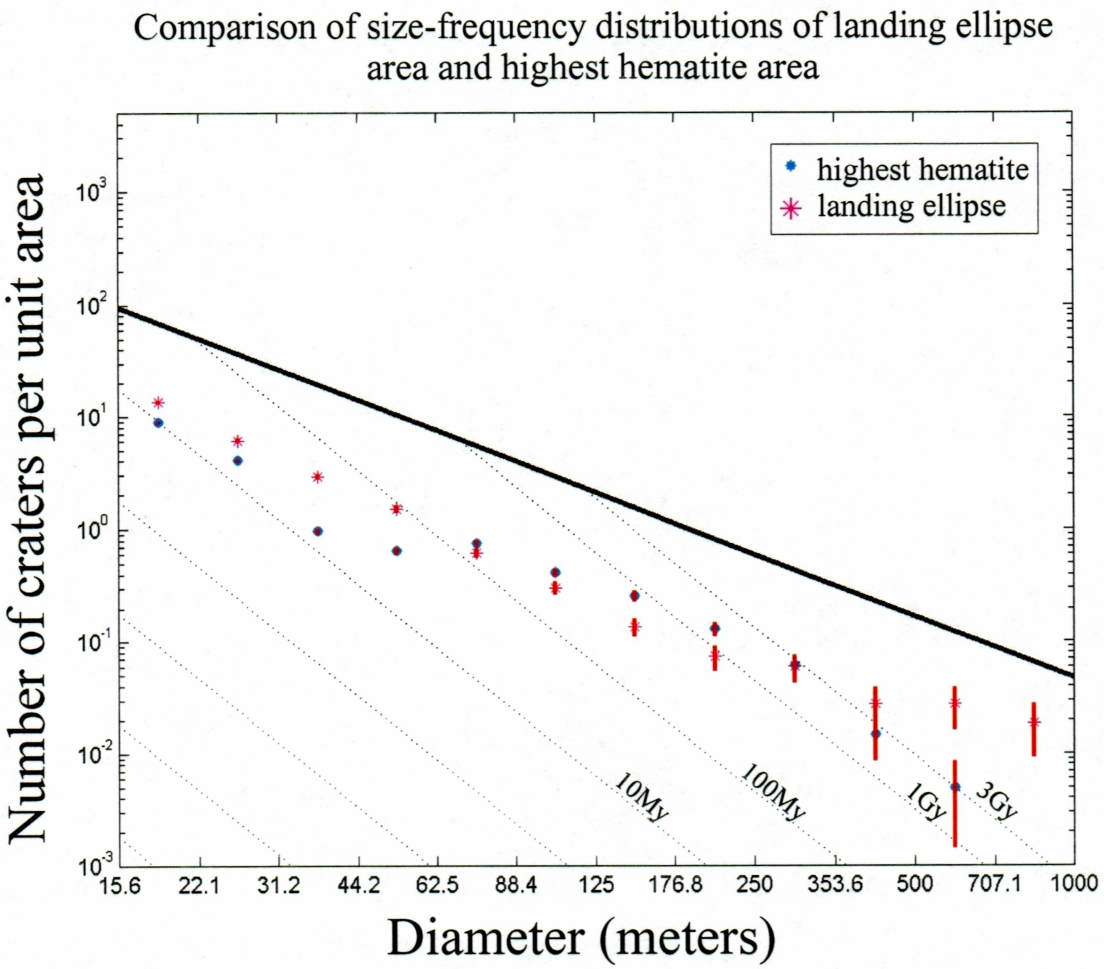

Figure 8: Comparison of size-frequency distributions of landing ellipse area and highest hematite area. The combined six images measured within the region of Meridiani that shows the strongest hematite concentration is shown with blue circles and the combined five images measured within the Opportunity landing ellipse is shown with magenta markers. The solid line represents saturation equilibrium and the light dashed lines are isochrons of various ages (after Hartmann, 2002). Error bars are shown in red.

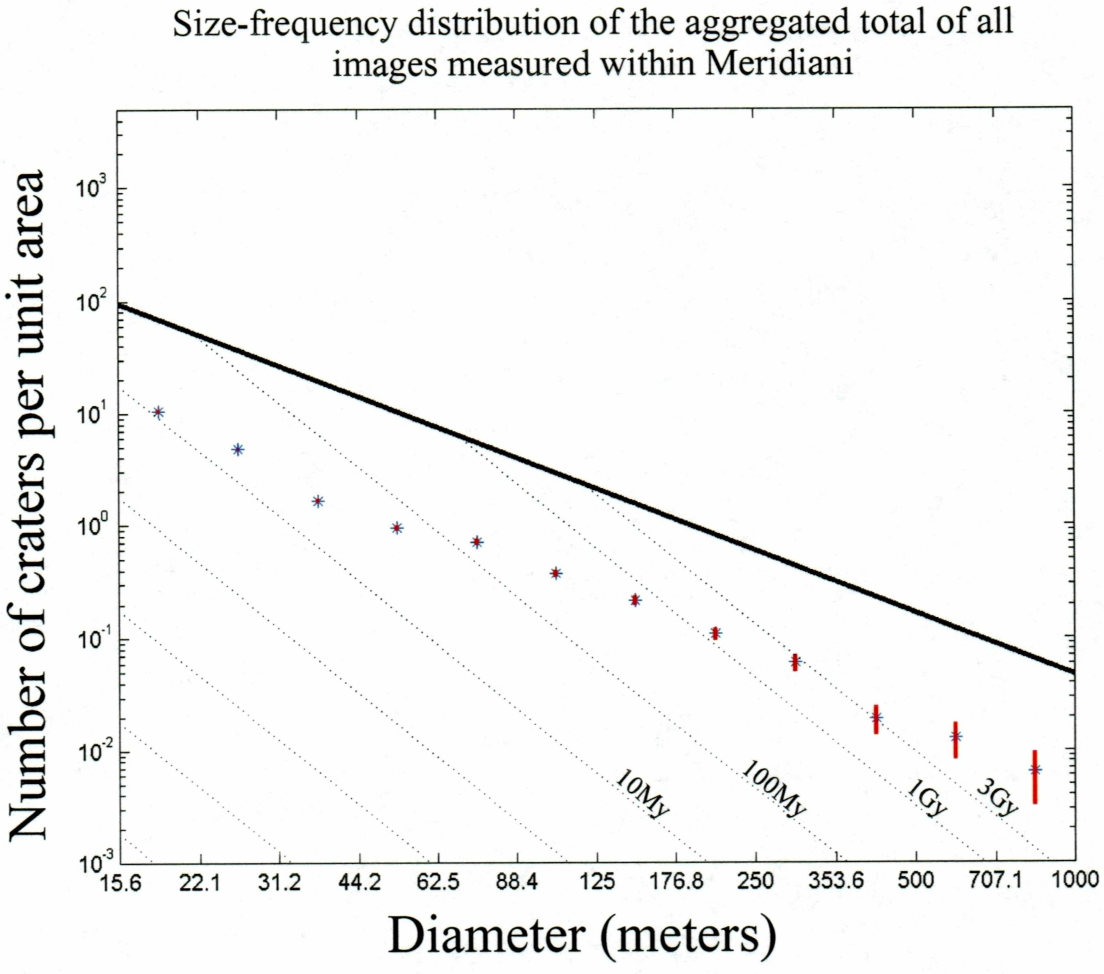

Figure 9: Size-frequency distribution of the aggregated total for all eleven images measured within Meridiani. The solid line represents saturation equilibrium and the light dashed lines are isochrons of various ages (after Hartmann, 2002). Error bars are shown in red.

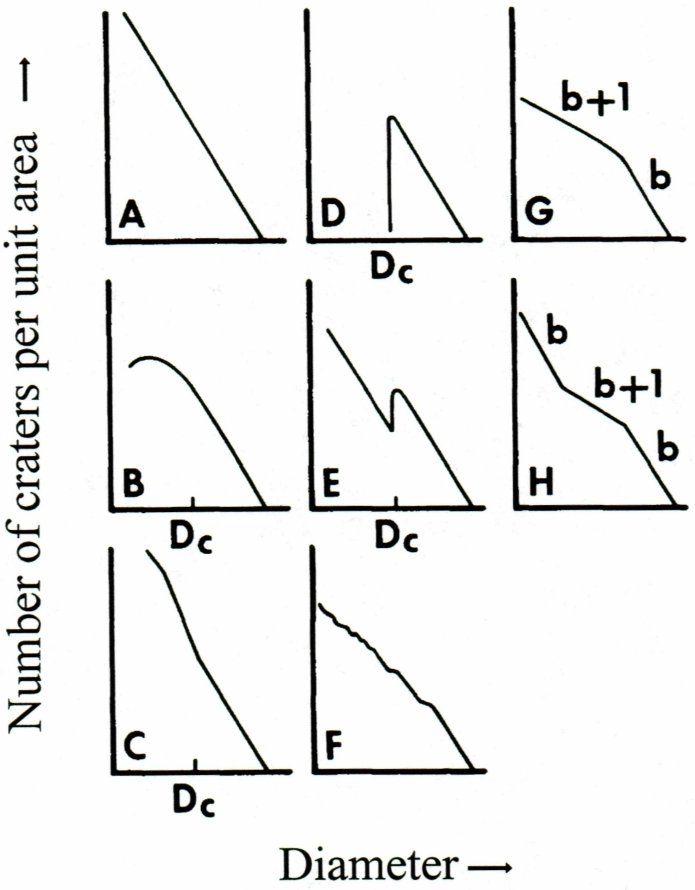

Figure 10: From Basaltic Volcanism Study Project (1981), theoretical models of possible variations among size-frequency distributions. A. Normal primary impact frequency distribution showing a production population with little geologic activity except cratering occurring. B. Turnover due to failure to resolve small craters, an observational error eliminated by rejecting data below an incompleteness limit. C. Addition of secondary impacts at small sizes causes an upward bend. D. Blanketing by a single layer of depth greater than d erases craters below a critical diameter, Dc, which are shallower than d. E. As in D, but after a period of time, when the blanket has been partially recratered. F. Successive episodes of ejecta blanketing and recratering, plus preferential removal of small craters builds an irregular curve bending over due to loss of small craters. G. Slow steady deposition of dust builds up a steady state with old shallower craters being obliterated faster than old larger craters; magnitude of slope is one less than production slope shown in A. H. As in G, but after slow deposition stops, allowing partial recratering.

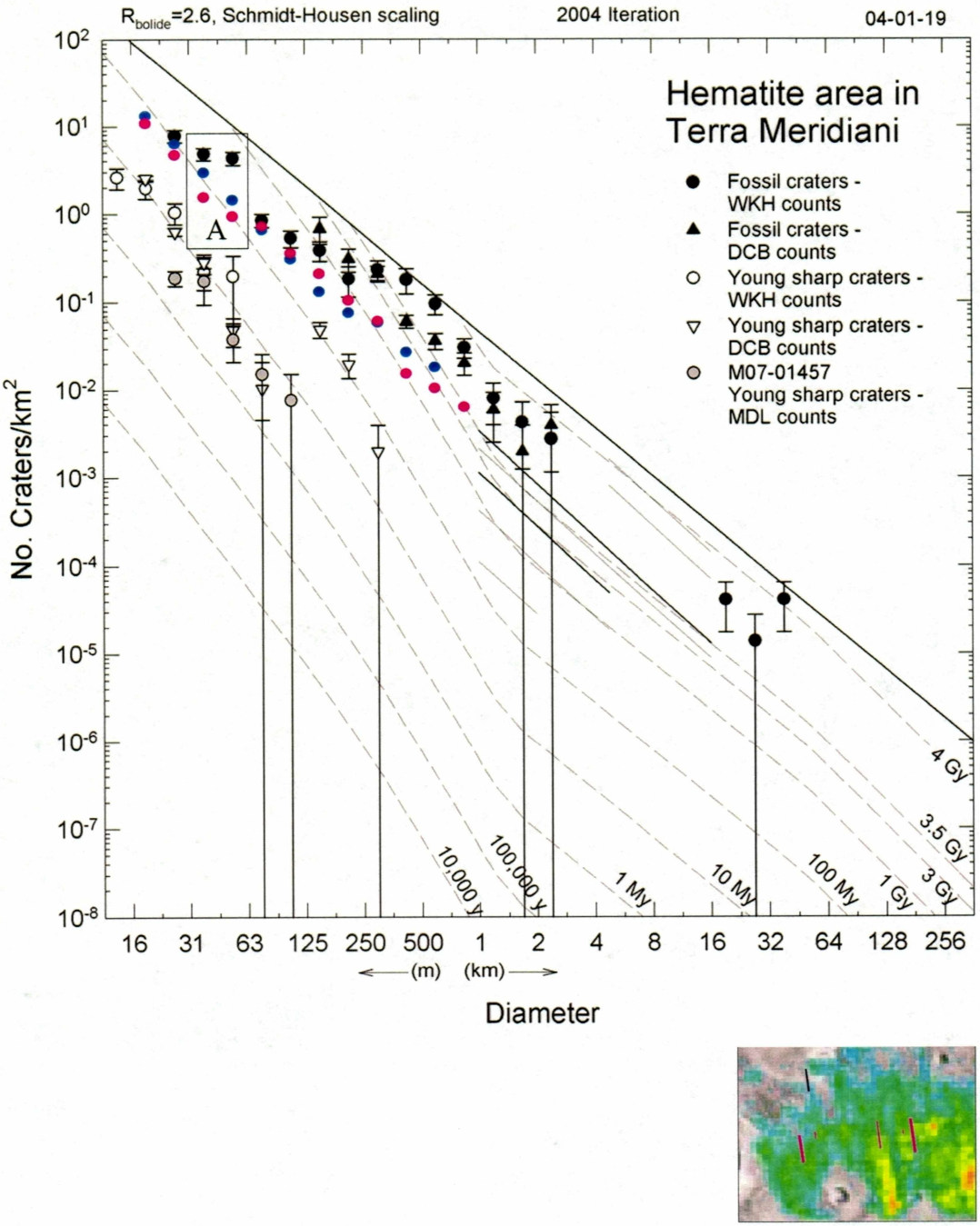

Figure 11a: Figure modified from Hartmann (2004) of size-frequency distribution from Meridiani with data from this study overlain. Figure 6 data (landing ellipse area) shown with blue circles (total area=219.5 km^2). Data from Figure 9 (entire study area) shown with magenta circles (total area=629.1 km^2). Hartmann's crater counts are from MOC-NA image m0001661 (7.04°S, 1.14°W, area=31.7 km^2, map scale=2.87 m/pixel). Inset shows location of m0001661 (black box) compared to location of images measured in this study (pink boxes).

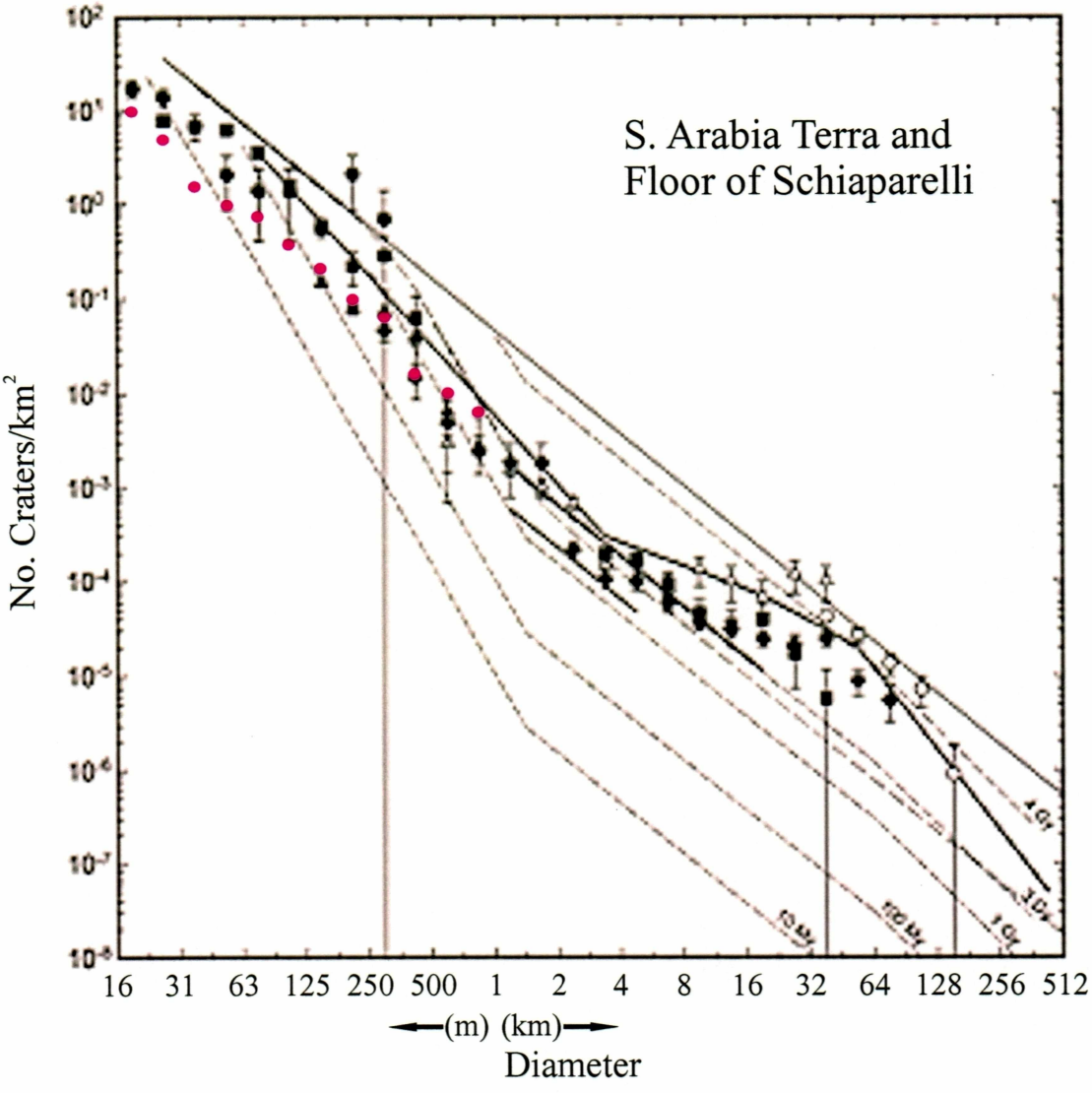

Figure 11b: Figure modified from Hartmann (2004) of size-frequency distribution from South Arabia Tera with data from this study overlain. Data from Figure 9 (entire study area) shown with magenta circles.

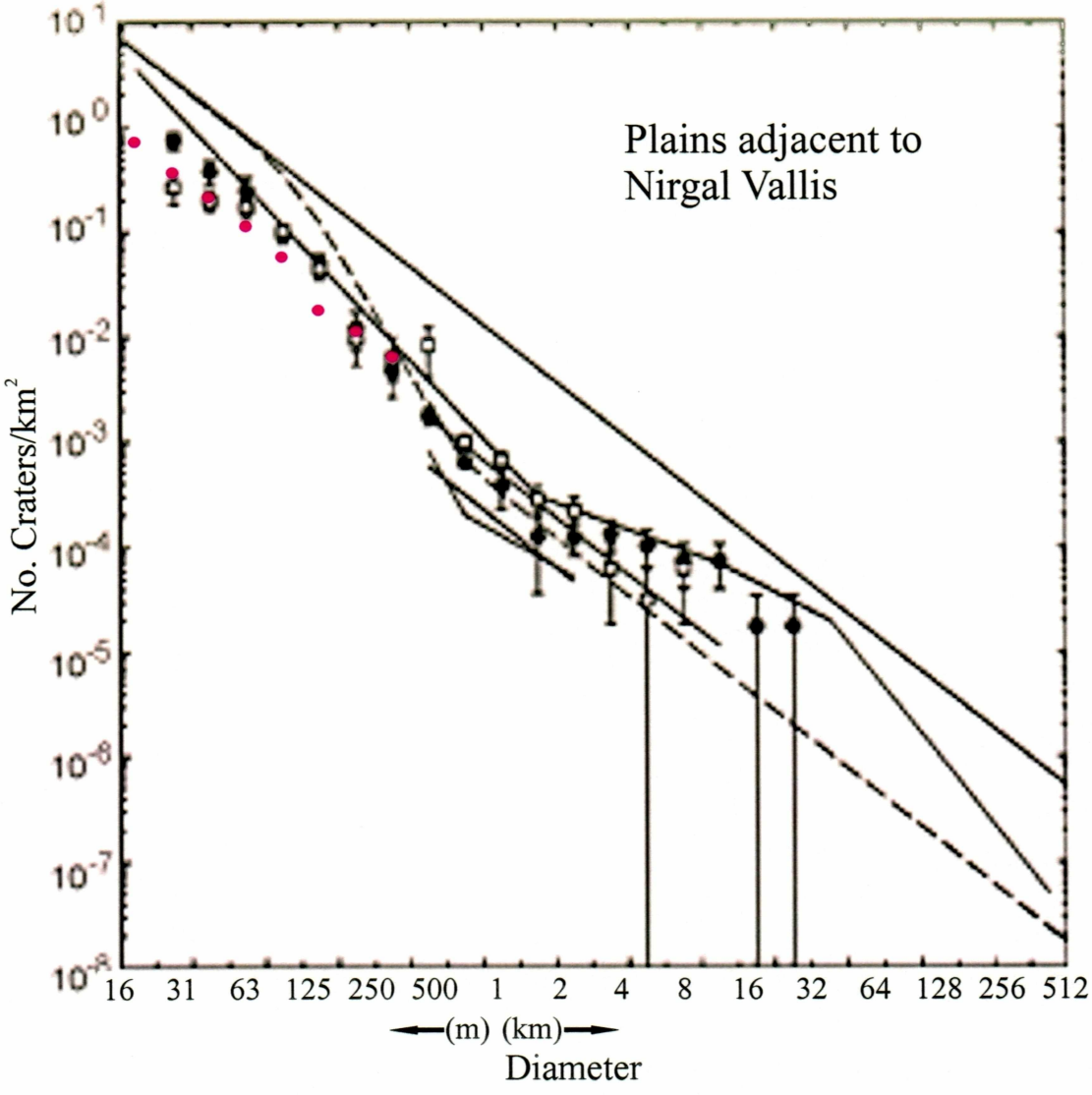

Figure 11c: Figure modified from Hartmann (2004) of size-frequency distribution from Nirgal Vallis with data from this study overlain. Data from Figure 9 (entire study area) shown with magenta circles.

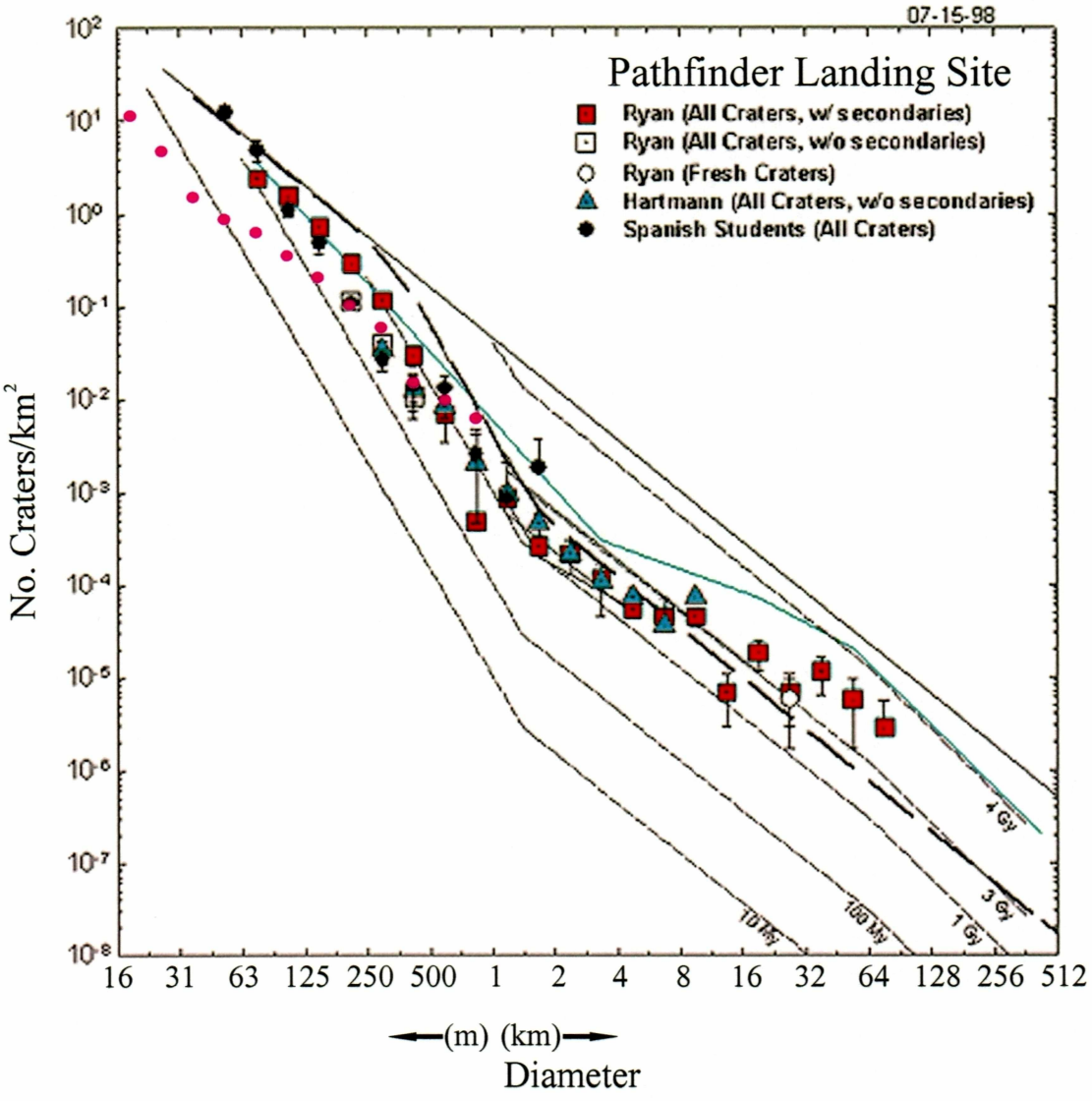

Figure 11d: Figure modified from Hartmann (2004) of size-frequency distribution from the Pathfinder landing site with data from this study overlain. Data from Figure 9 (entire study area) shown with magenta circles.

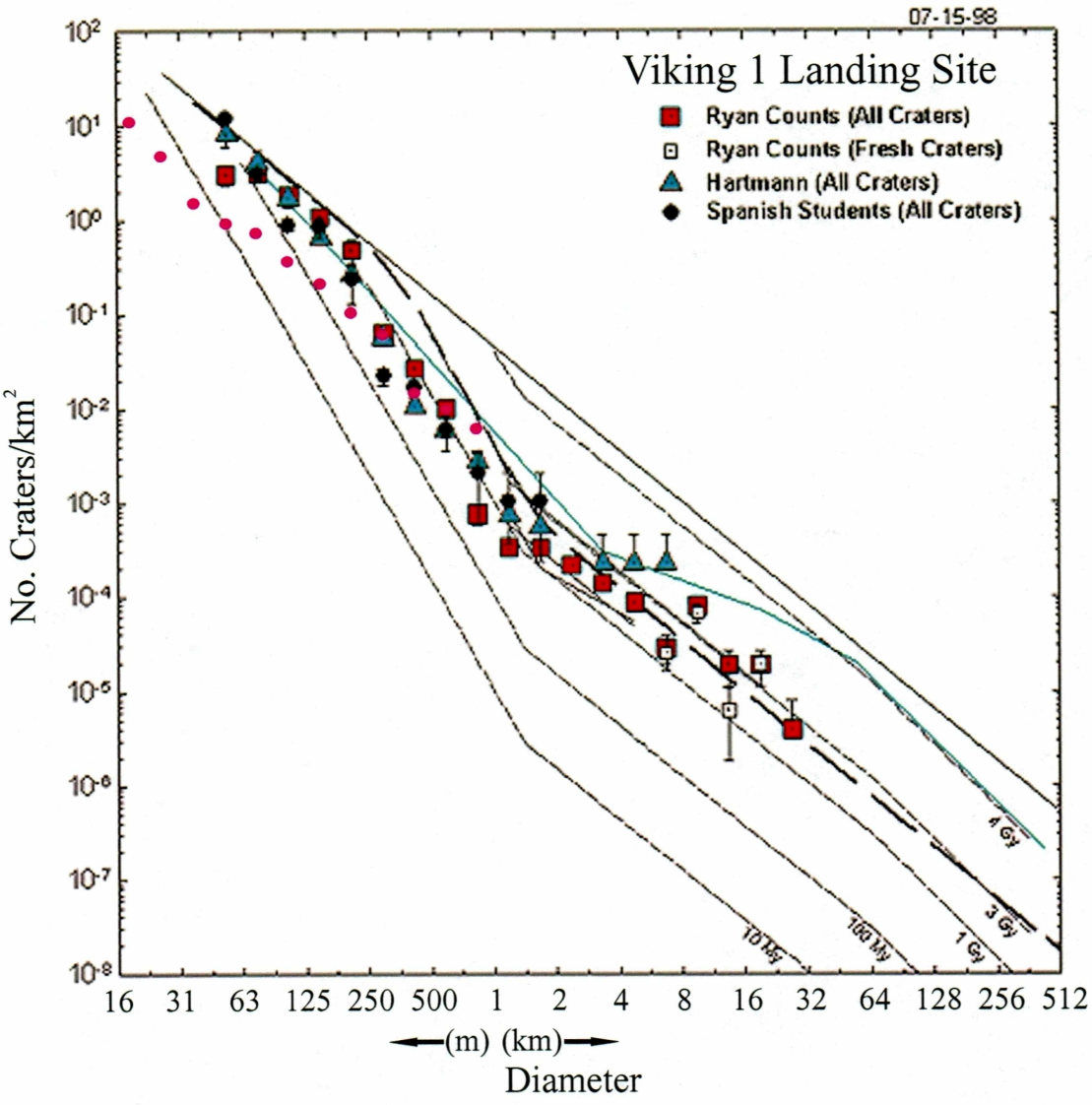

Figure 11e: Figure modified from Hartmann (2004) of size-frequency distribution from the Viking 1 landing site area with data from this study overlain. Data from Figure 9 (entire study area) shown with magenta circles.

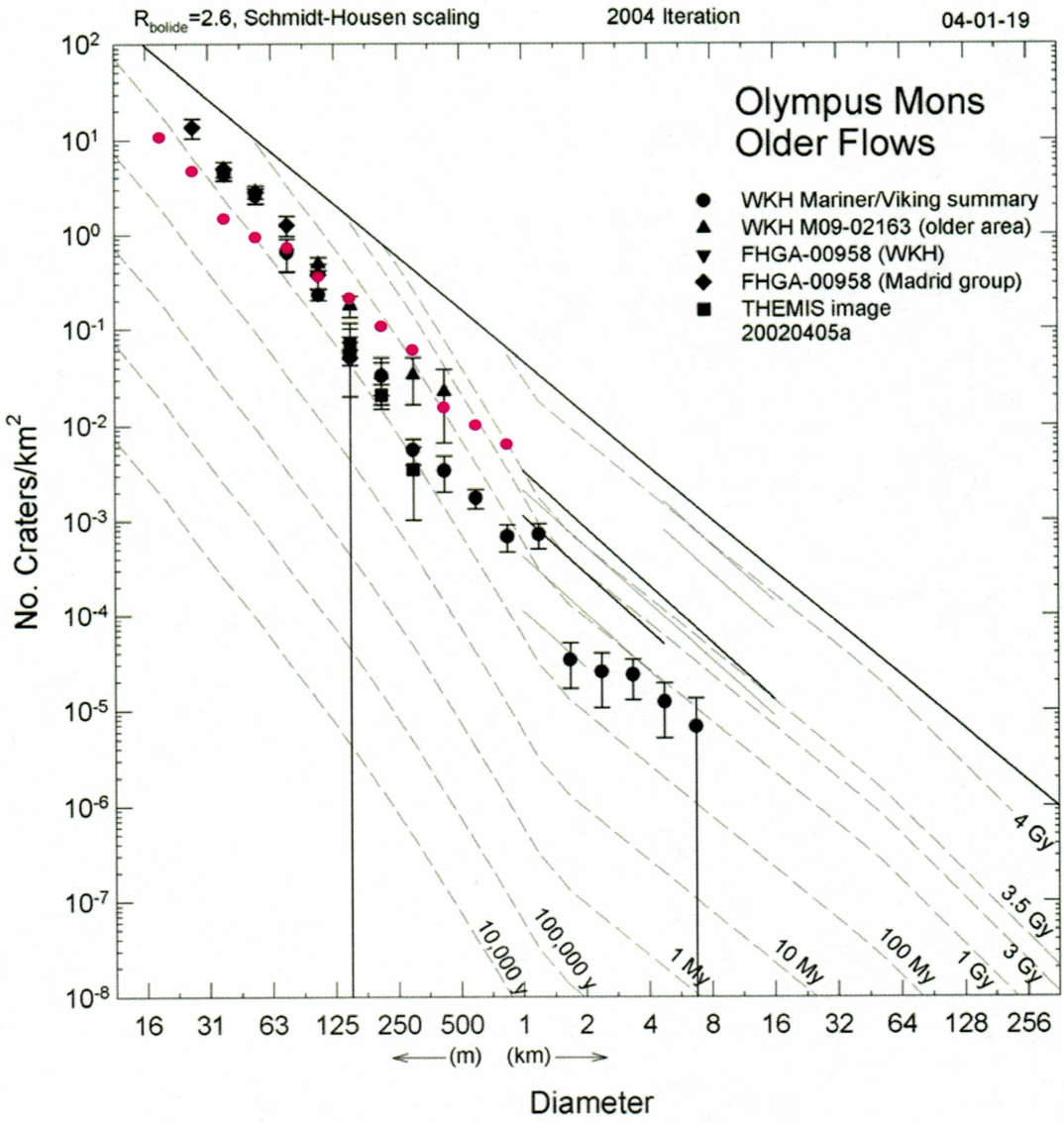

Figure 11f: Figure modified from Hartmann (2004) of size-frequency distribution from the Olympus Mons older lava flows with data from this study overlain. Data from Figure 9 (entire study area) shown with magenta circles.

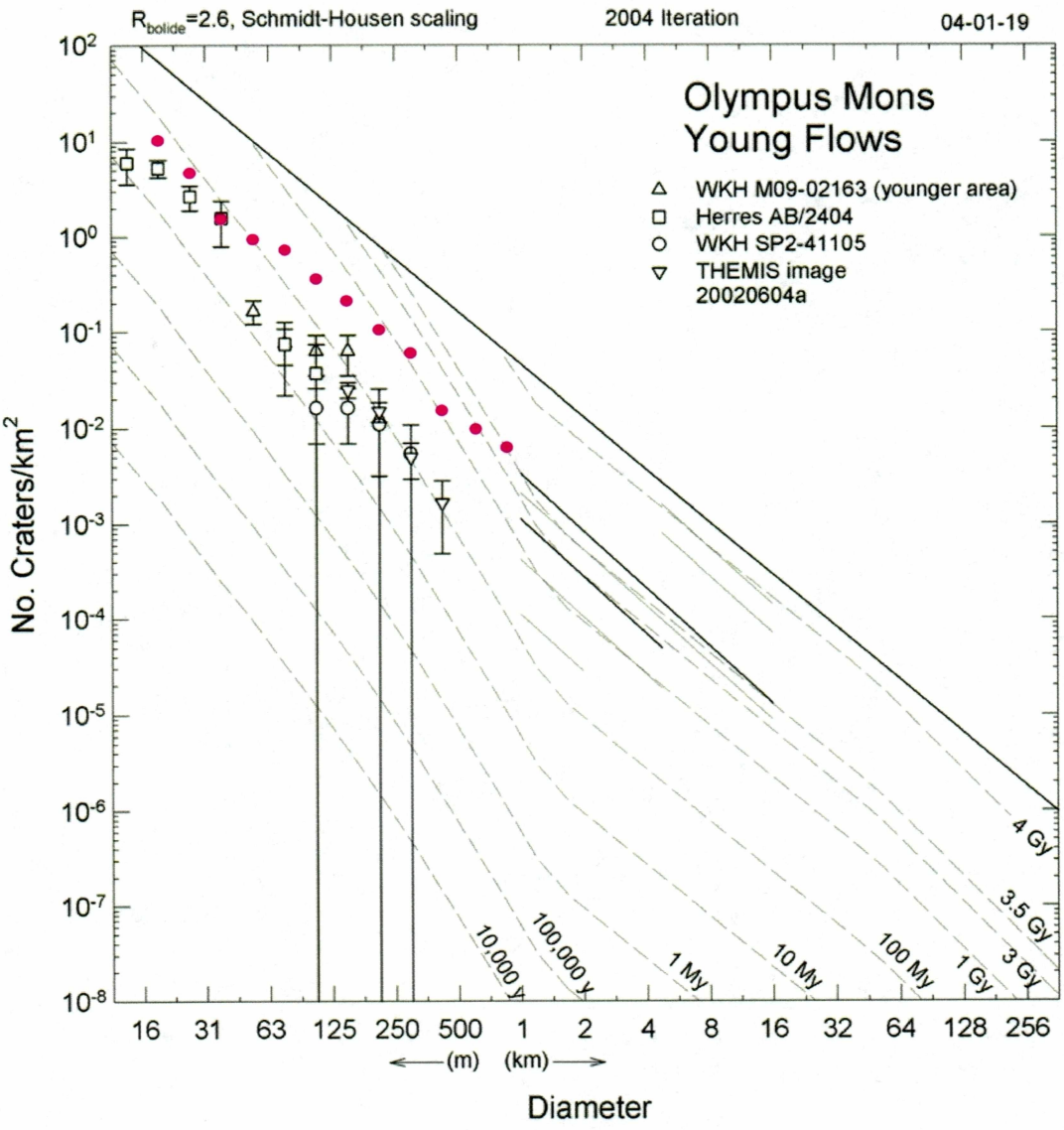

Figure 11g: Figure modified from Hartmann (2004) of size-frequency distribution from the Olympus Mons young lava flows with data from this study overlain. Data from Figure 9 (entire study area) shown with magenta circles.

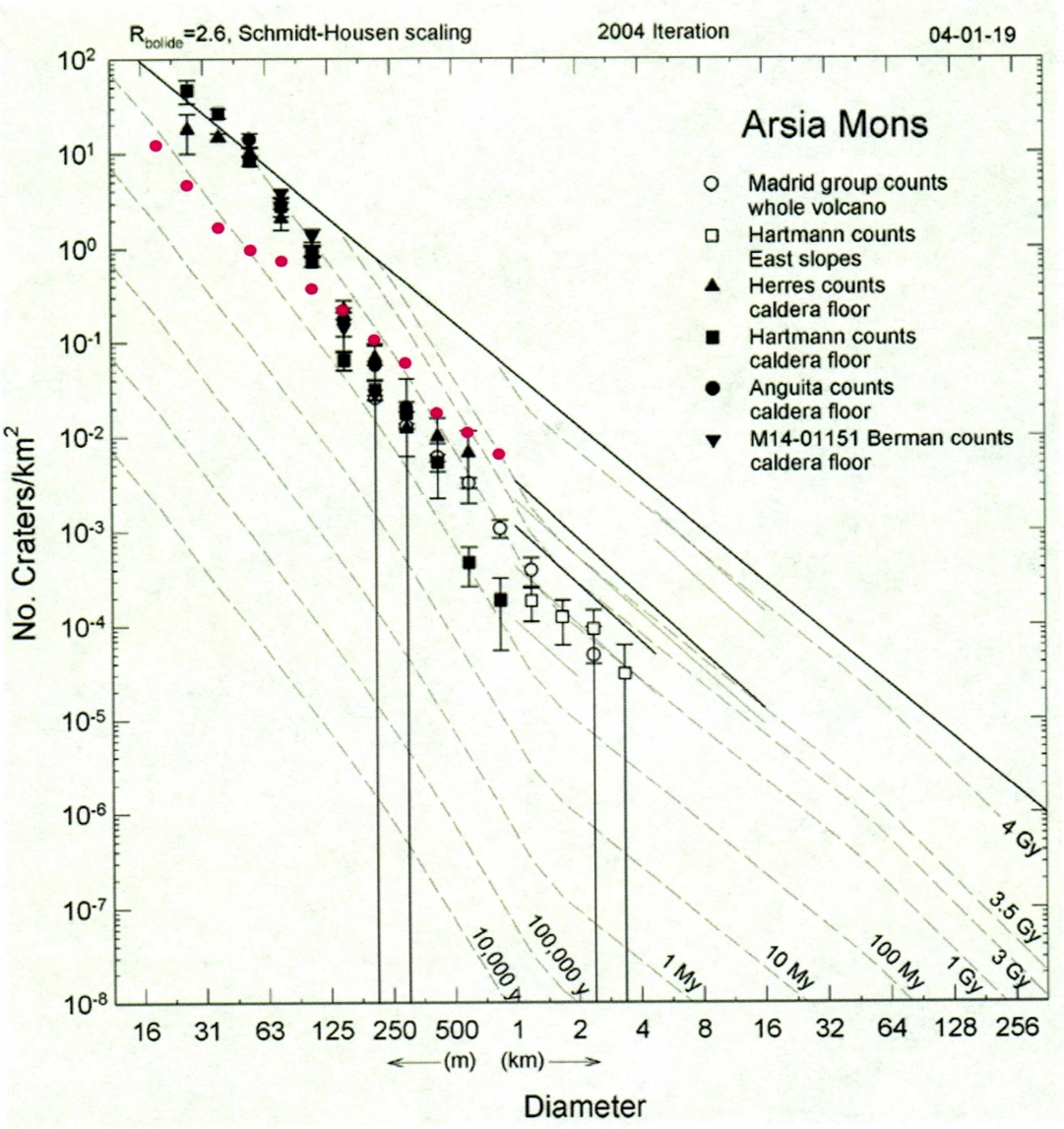

Figure 11h: Figure modified from Hartmann (2004) of size-frequency distribution from Arsia Mons with data from this study overlain. Data from Figure 9 (entire study area) shown with magenta circles.

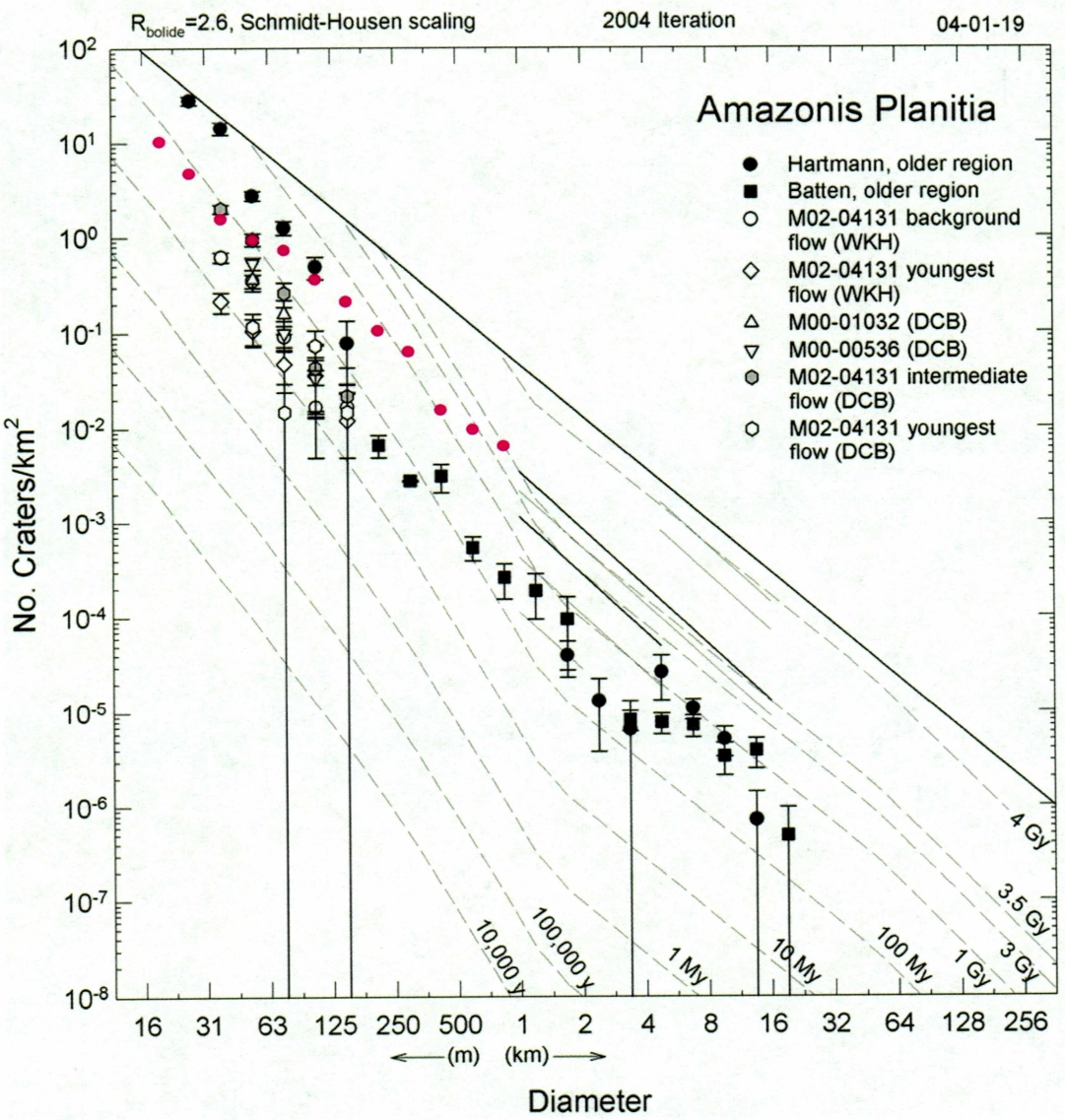

Figure 11i: Figure modified from Hartmann (2004) of size-frequency distribution from Amazonis Planitia with data from this study overlain. Data from Figure 9 (entire study area) shown with magenta circles.

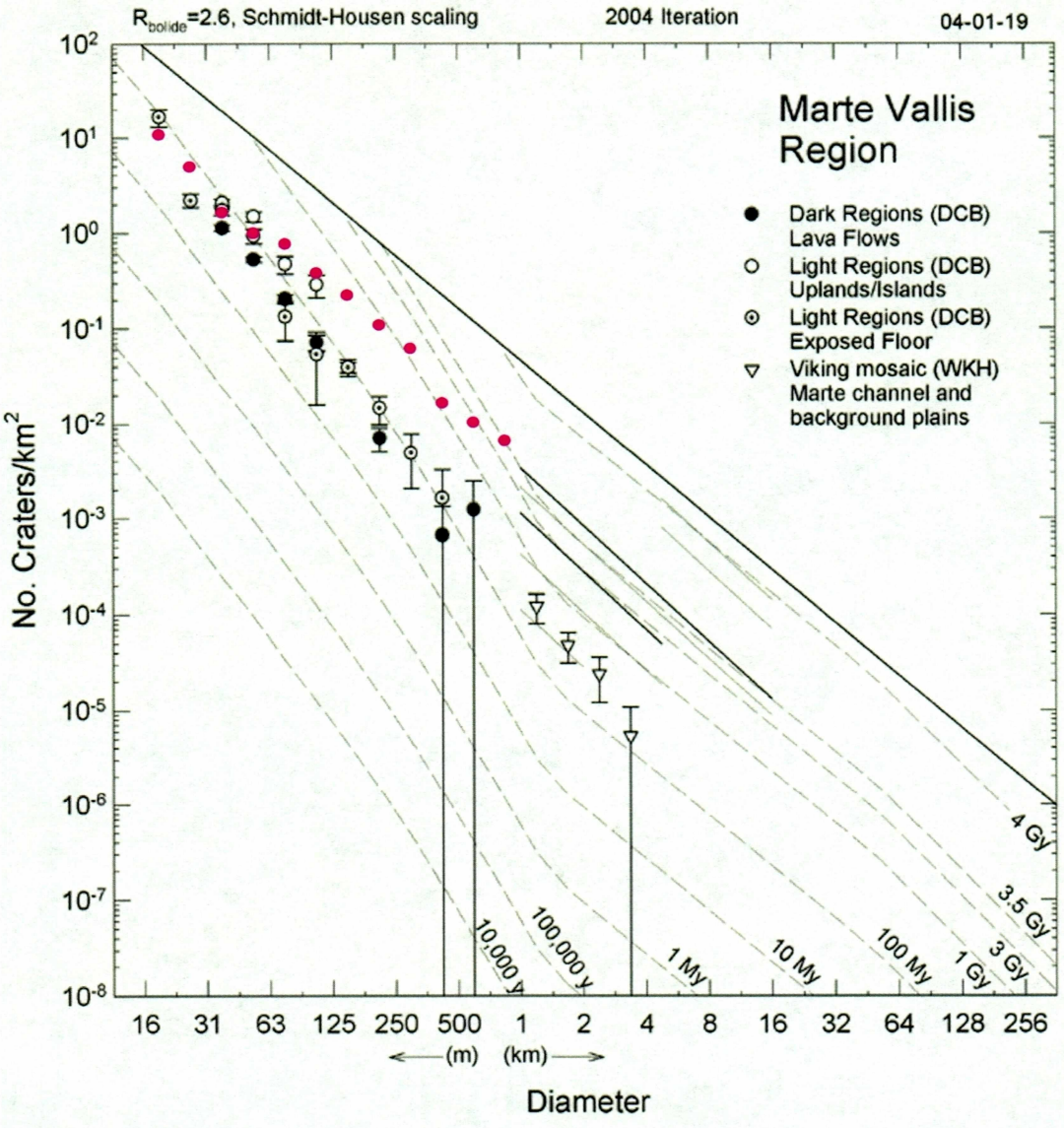

Figure 11j: Figure modified from Hartmann (2004) of size-frequency distribution from Marte Vallis with data from this study overlain. Data from Figure 9 (entire study area) shown with magenta circles.

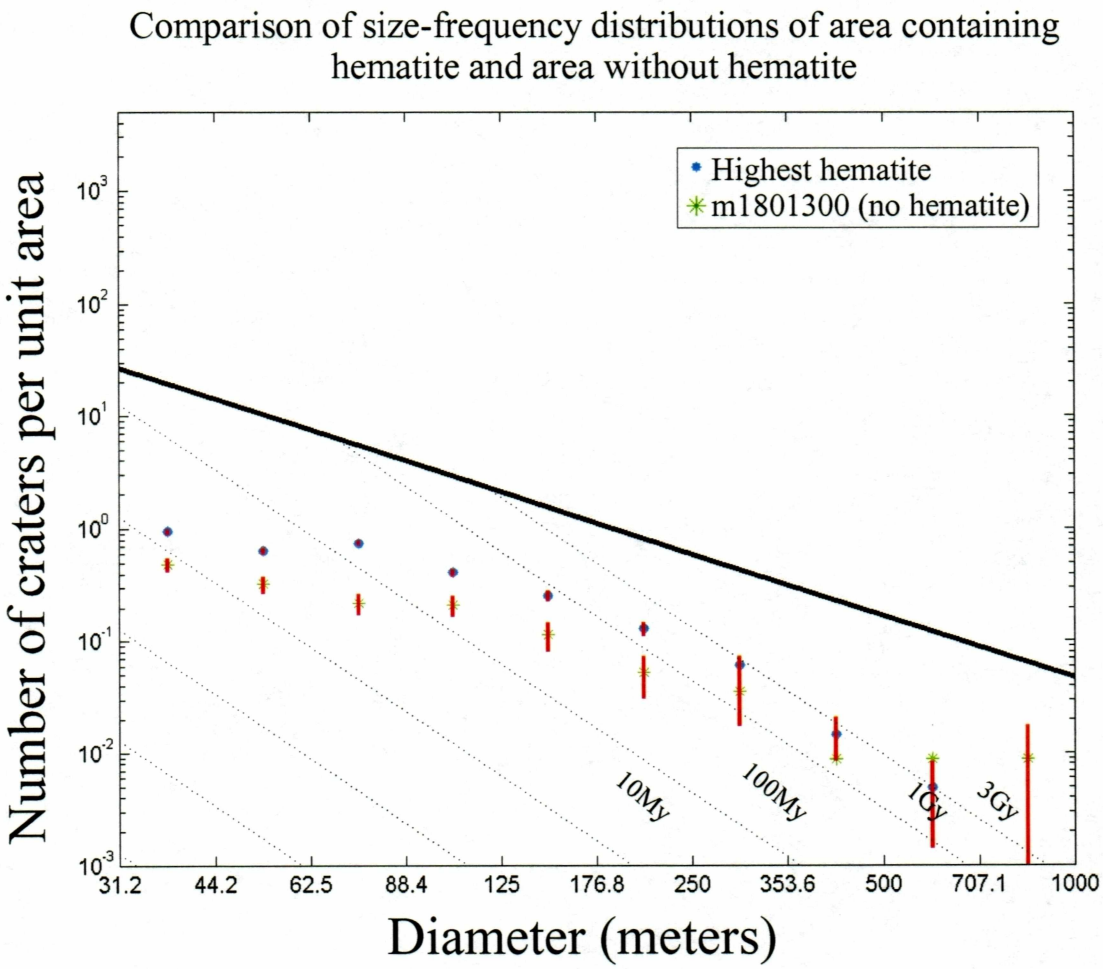

Figure 12: Size-frequency distribution for m1801300 (green markers) overlain with the size-frequency distribution for the aggregated total of the six images measured within the region of Meridiani that shows the strongest hematite concentration (blue circles). The solid line represents saturation equilibrium and the light dashed lines are isochrons of various ages (after Hartmann, 2002). Error bars are shown in red. MOC-NA image m1801300 occurs 350 km from the eastern boundary of the hematite signature (0.14°S, 5.92°E). Its area is 113.7 km^2, map scale = 5.82 m/pixel, and number of craters counted is 350.

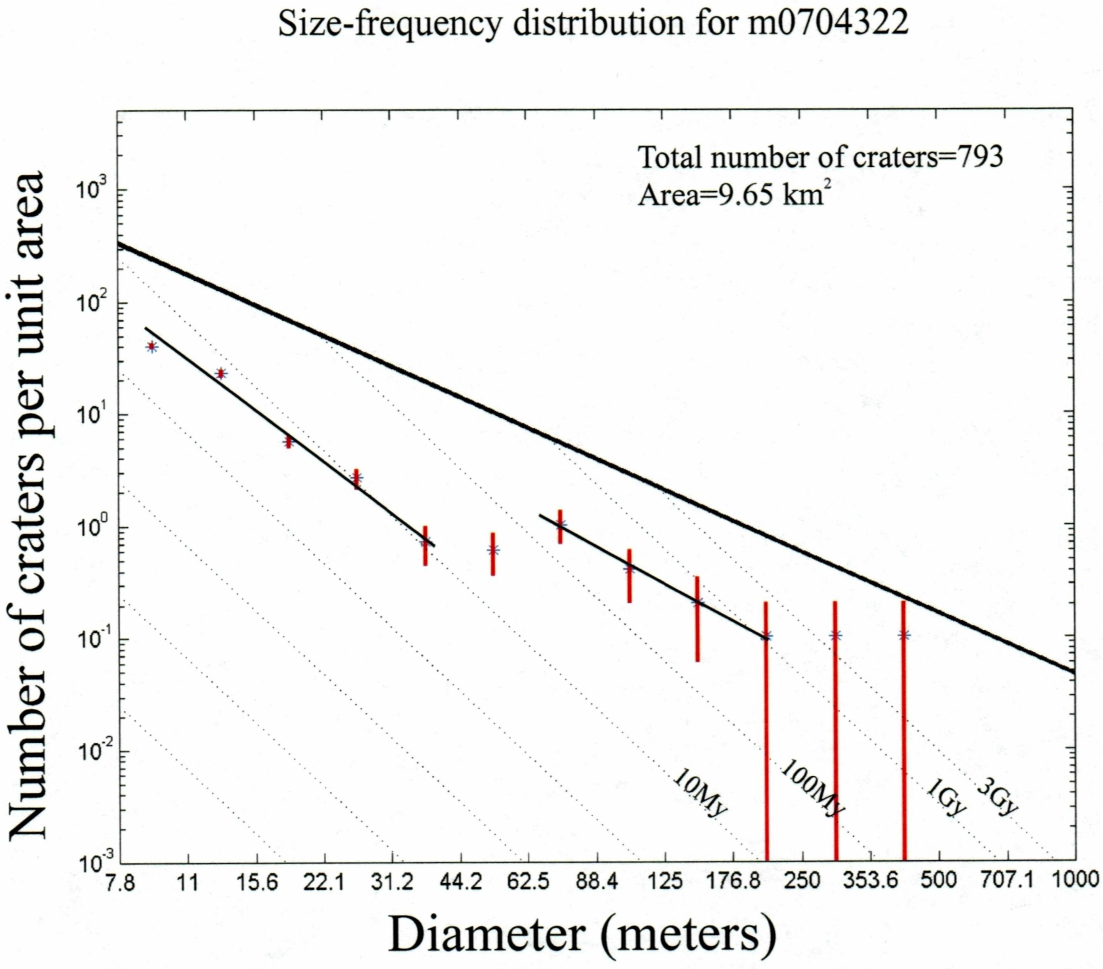

Figure 13: Size-frequency distribution for m0704322. The solid line represents saturation equilibrium and the light dashed lines are isochrons of various ages (after Hartmann, 2002). The light solid line is the fit to the data. Error bars are shown in red. Because the map scale of this image is 1.45 m/pixel, the minimum diameter shown on the size-frequency distribution is 7.8 m.

Figure 14: Mars Orbiter Camera Narrow Angle image m0704322. This image has been processed in ISIS according to the procedure found in Figure 3 and projected using sinusoidal projection. The image is located at 2.83°S, 3.79°E; map scale=1.45 meters/pixel; area=9.65 km^2.

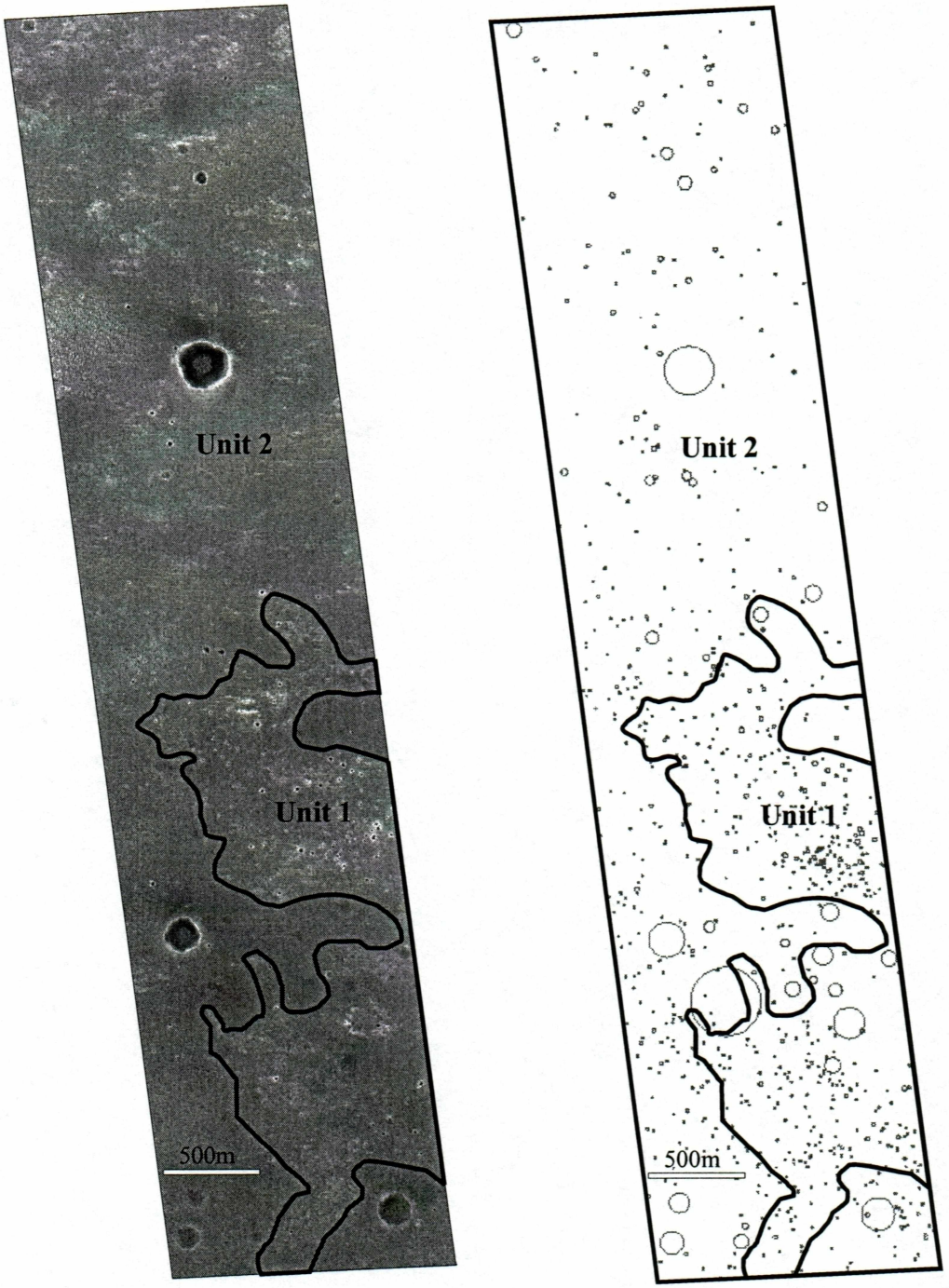

Figure 15: Mars Orbiter Camera Narrow Angle image m0704322 showing the identification and location of two surface units, Unit 1 and Unit 2. The right image area shows the outline of the craters counted within each surface unit.

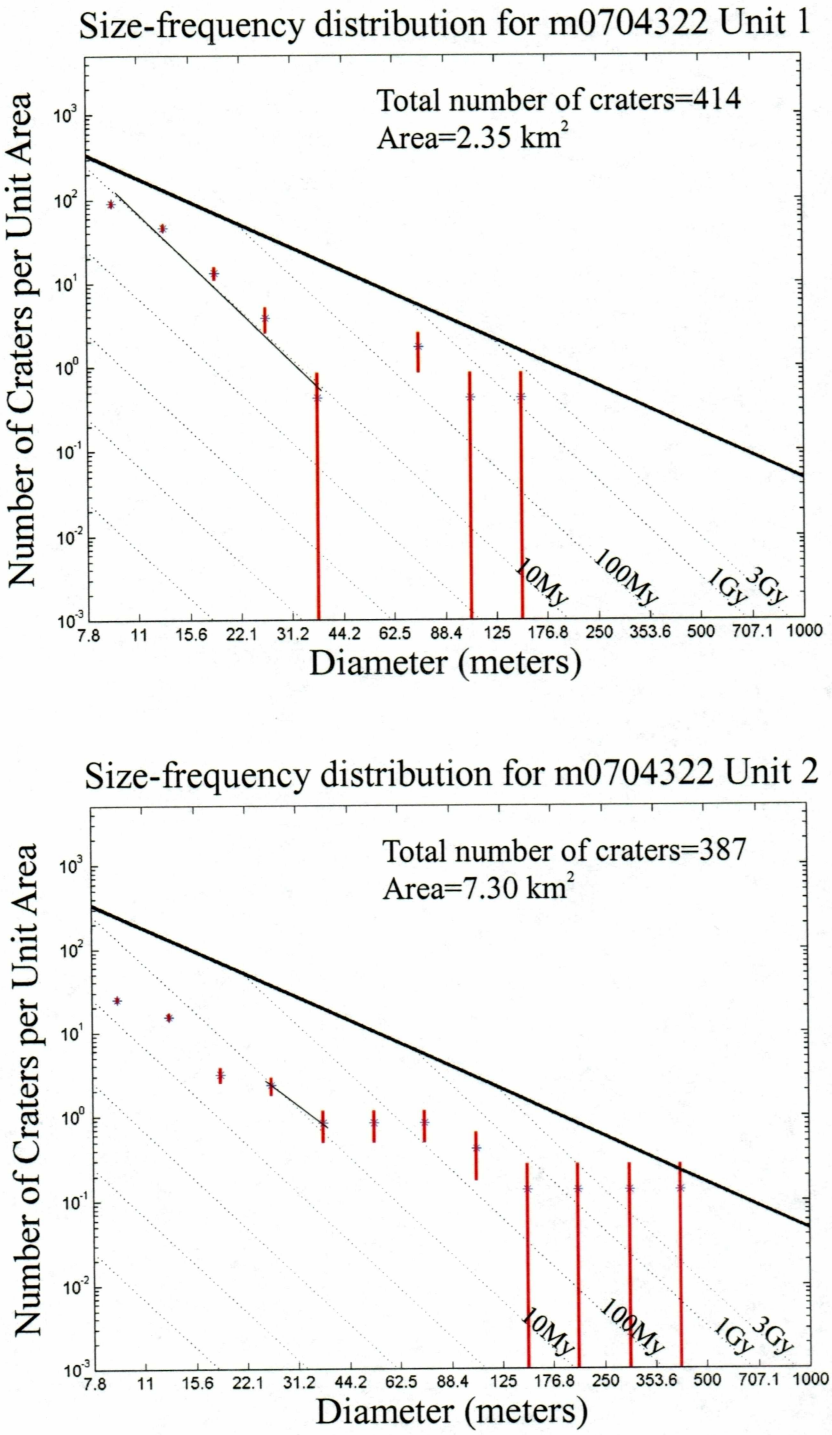

Figure 16: Size-frequency distribution for m0704322 Unit 1 and Unit 2. The solid line represents saturation equilibrium and the light dashed lines are isochrons of various ages (after Hartmann, 2002). The light solid line is the fit to the data. Error bars are shown in red. Unit 0, the ancient mostly buried unit, can be seen poking through surface units 1 and 2 at the larger diameters.

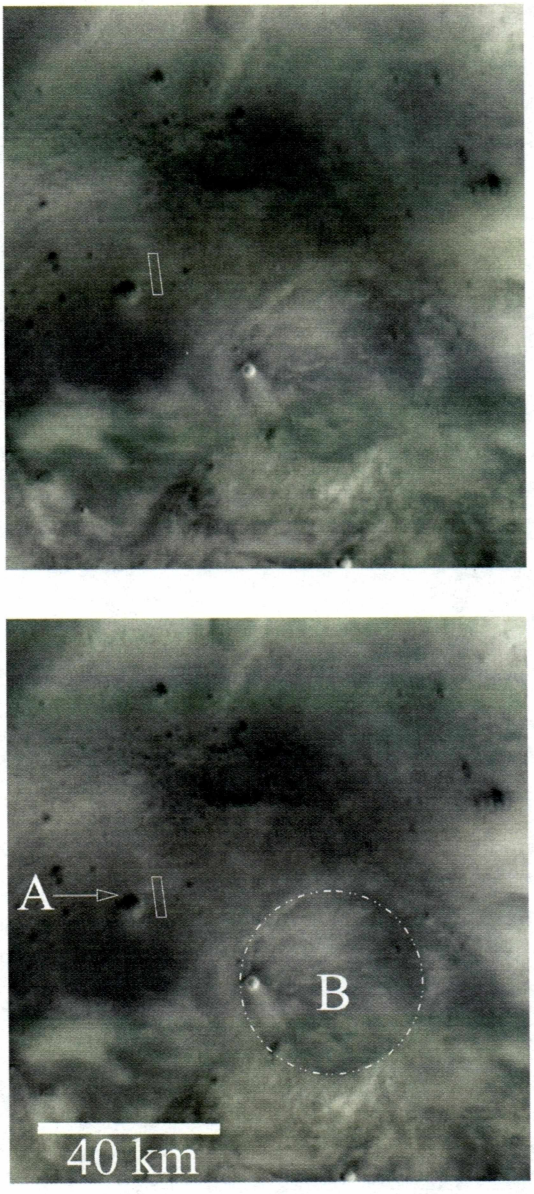

Figure 17: Wide angle context image for m0704322. Map scale=250m/pixel. Small white rectangular box indicates size and location of MOC-NA image m0704322. The image lies ~5 km east of a 5-6 km impact crater, labeled as feature A in the bottom image and ~25 km northwest of a 40 km impact crater, labeled as feature B. Top and bottom image are identical but both are shown for ease of identifying features A and B.

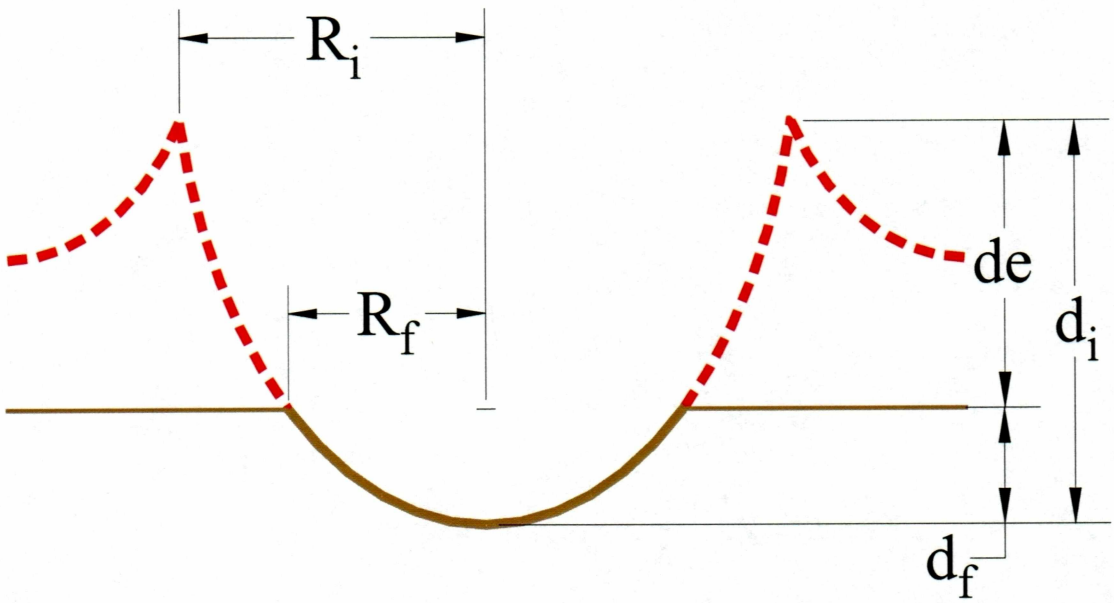

Figure 18: Diagram of crater showing variables for erosion equation. Erosion will decrease the apparent diameter of a crater. The red dashed line shows the original crater profile prior to any erosion with radius, R_i. The brown solid line shows the profile of the crater as it exists today with radius, R_f. The original crater of depth, d_i, over a period of time has undergone an amount of erosion, de. Its residual depth is d_f, where subscript i denotes the initial condition of the crater and subscript f denotes the final or current condition of the crater.

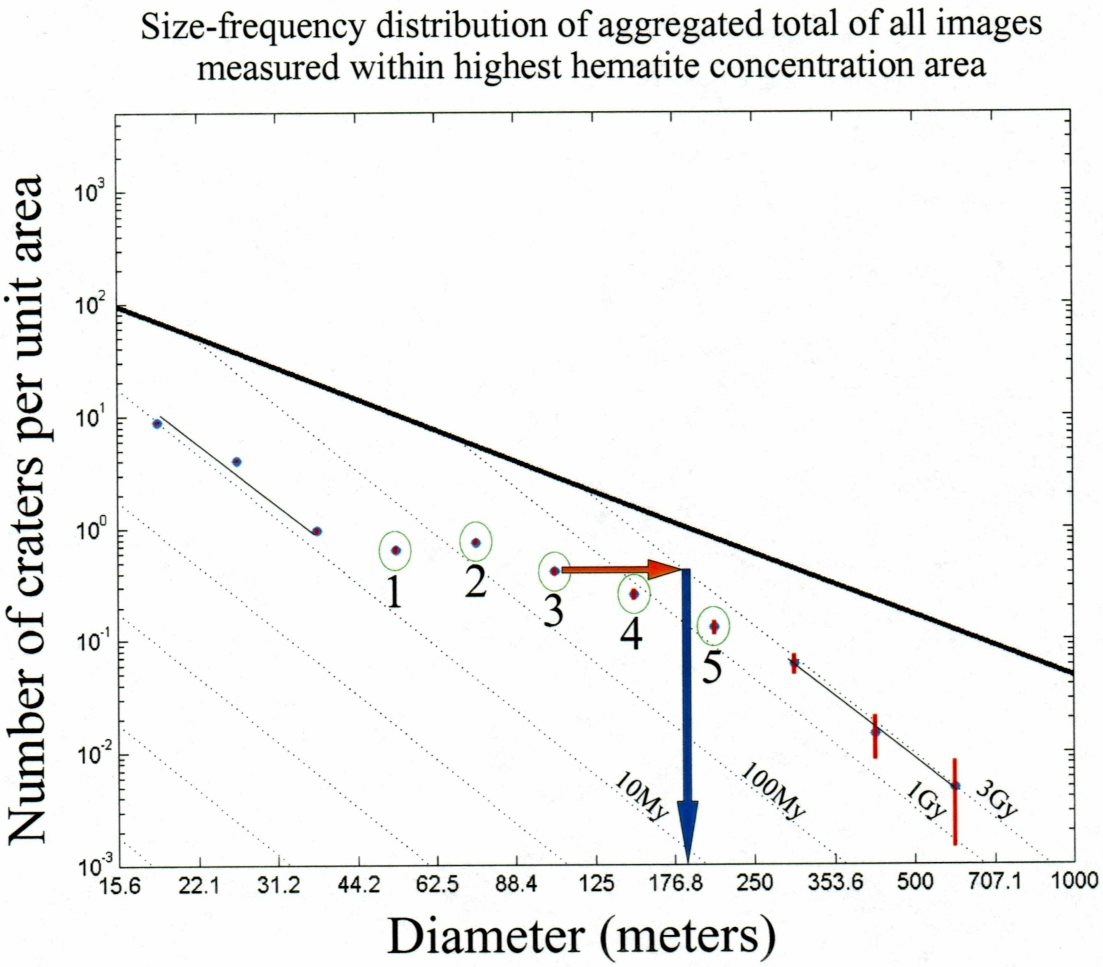

Figure 19: Graphical example of steps taken to find permissible depth of erosion. First the number of craters in the bin per area (N) is found (orange arrow) and then this number is used in equation 2, Hartmann's isochron equation, to find at what diameter this density would occur on the 3 Gy isochron (blue arrow). The five points shown with green ellipses occur between the trend found at the 10 My isochron and the 3 Gy isochron, shown with light solid lines and correspond with Table 5.

Table 1: List of information for each image within study. N is the number of craters measured in the image. *The % hematite is approximated qualitatively. Images a through e are within the landing ellipse for the Mars Exploration Rover Opportunity and images f through k occur within the area of highest hematite concentration (see Figure 1). Corresponding size-frequency distributions are found in Figures 4a-4k.

Image	Center Longitude	Center Latitude	Map Scale (meters/pixel)	*~ % Fe_2O_3	Area (km^2)	N
a) E0101056	7.15	-2.28	2.880	7	77.65	2690
b) M0001660	6.92	-2.05	1.816	6	10.40	418
c) E0500801	5.87	-2.04	3.291	8	40.17	1671
d) M0802647	5.47	-2.00	1.822	8	6.28	217
e) E0200373	5.31	-2.06	3.662	7	85.01	2849
Total for area within landing ellipse for MER Opportunity					219.51	7845
f) M0704322	3.79	-2.83	1.452	11	9.65	793
g) E0300624	3.43	-2.53	3.650	13	85.49	2773
h) E0301946	2.93	-2.48	3.645	10	103.94	2377
i) E0201143	2.71	-2.52	3.665	11	71.45	806
j) E0402072	2.38	-2.51	3.653	10	64.60	804
k) E0503058	2.12	-1.99	3.648	12	74.41	1142
Total for area within highest hematite concentration					409.54	8695
Total					629.06	16540

Table 2: Number of craters within each diameter bin. Images a through e are within the landing ellipse for MER Opportunity and images f through k occur within the area of highest hematite concentration (Figure 1). Corresponding size-frequency distributions are found in Figures 4a-4k.

	Landing ellipse images							Highest hematite concentration images						
Diameter Bins	a) e01-01056	b) m00-01660	c) e05-00801	d) m08-02647	e) e02-00373	total landing	total highest	f) m07-04322	g) e03-00624	h) e03-01946	i) e02-01143	j) e04-02072	k) e05-03058	All
2.0-2.8	0	0	0	0	0	0	0	0	0	0	0	0	0	0
2.8-3.9	0	0	0	0	0	0	0	0	0	0	0	0	0	0
3.9-5.5	0	4	0	0	0	4	3	3	0	0	0	0	0	7
5.5-7.8	7	12	0	7	0	26	66	66	0	0	0	0	0	92
7.8-11.0	187	99	8	79	16	389	466	389	41	21	2	2	11	855
11.0-15.6	919	206	259	80	437	1901	1587	222	727	376	103	43	116	3488
15.6-22.1	939	62	824	20	1106	2951	3602	55	1268	1084	388	308	499	6553
22.1-31.2	364	18	371	9	567	1329	1646	26	336	553	150	289	292	2975
31.2-44.2	121	13	135	13	355	637	392	7	89	135	39	49	73	1029
44.2-62.5	79	2	49	6	193	329	264	6	89	61	43	21	44	593
62.5-88.4	41	0	12	2	82	137	309	10	99	76	45	33	46	446
88.4-125.0	15	1	10	0	41	67	169	4	53	38	21	30	23	236
125.0-176.8	7	0	0	0	23	30	105	2	35	20	10	16	22	135
176.8-250.0	1	0	0	1	14	16	53	1	23	10	2	9	8	69
250.0-353.5	2	0	1	0	10	13	25	1	12	0	2	4	6	38
353.5-500.0	4	0	0	0	2	6	6	1	1	2	1	0	1	12
500.0-707.1	2	1	2	0	1	6	2	0	0	1	0	0	1	8
707.1-1000	2	0	0	0	2	4	0	0	0	0	0	0	0	4
	2690	418	1671	217	2849	7845	8695	793	2773	2377	806	804	1142	16540

Table 3: Determination of minimum diameter of crater to be graphed on size-frequency distributions. The map scale of each image is multiplied by 4, the minimum number of pixels needed to identify a crater.

Image	Map Scale (meters/pixel)	Map Scale times 4
M0704322	1.452	5.806
M0001660	1.816	7.265
M0802647	1.822	7.287
E0101056	2.880	11.521
E0500801	3.291	13.162
E0301946	3.645	14.581
E0503058	3.648	14.591
E0300624	3.650	14.600
E0402072	3.653	14.614
E0200373	3.662	14.648
E0201143	3.665	14.659

Table 4: Characteristics of the landing ellipse area as compared to the highest hematite concentration area.

Landing Ellipse Area	Highest Hematite Area
• more gradual decrease in crater density (fewer craters) from 62.5 to 250 meters • 62% more craters in 31.2 m bin • 2 craters greater than 500 meters • area of 409.5 km^2	• more dramatic decrease in crater density from 62.5 to 250 meters • small but significant dip from $30m < D < 60$ m • 10 craters greater than 500 meters • area of 219.5 km^2 • small (D>40m) diameter trend along the 10 My isochron • $70 m < D < 200$ m slope b+2

Table 5: Calculation of average depth of erosion in the Meridiani region. Points 1 through 5 are seen in figure 19. The original crater diameter prior to any erosion is D_i, where subscript i denotes the initial condition of the crater found on the 3 Gy, an assumed production function where erosion has not yet occurred. This value is calculated using N, the number of craters per unit area or crater density in Hartmann's 3 Gy isochron equation (2002). D_f denotes the crater diameter as it exists today where subscript f represents the final or current condition of the crater. The original crater over a period of time has undergone an amount of erosion, de, calculated using the depth of erosion equation.

Point	D_f	N	D_i	de
1	52.56	0.1655	165.53	29.77
2	74.33	0.1588	158.85	24.81
3	105.11	0.1860	186.03	25.33
4	148.65	0.2107	210.71	21.17
5	210.22	0.2520	252.01	15.33
			Average	23.28

LITERATURE CITED

Arvidson, R., J. Boyce, C. Chapman, M. Cintala, M. Fulchignoni, H. Moore, G. Neukum, P. Schultz, L. Soderblom, R. Strom, and A. Woronow, Crater Analysis Techniques Working Group, Standard Techniques for Presentation and Analysis of Crater Size-Frequency Data, *NASA Technical Memorandum* 79730, 20 pp., 1977.

Basaltic Volcanism Study Project: Hartmann, W. K., R.G. Strom, R.A.F. Grieve, S.J. Weidenschilling, J. Diaz, K.R. Blasius, C.R. Chapman, A. Woronow, E.M. Shoemaker, M.R. Dence, K.L. Jones, Chapter 8: Chronology of planetary volcanism by comparative studies of planetary cratering, in *Basaltic Volcanism on the Terrestrial Planets.* Pergamon Press, Inc., New York. 1286 pp., 1981.

Block, K. M. and N. G. Barlow, Secondary cratering rates on the basaltic plains of Mars and the Moon, in *Lunar Planet. Sci., XXXVI*, Abstract #1816, Lunar and Planetary Institute, Houston (CD-ROM), 2005.

Carr, M.H., *Water on Mars*, 229 pp., Oxford University Press, 1996.

Chapman, C.R., Cratering on Mars: I. Cratering and obliteration history, *Icarus* 22, 272-291, 1974.

Chapman, C. R., and K. L. Jones, Cratering and obliteration history of Mars, *Ann. Rev.Earth Planet. Sci.*, 5, 515 – 540, 1977.

Chappelow, J. E. and V. L. Sharpton, An Improved Shadow Measurement Technique for Constraining the Morphometry of Simple Impact Craters, *Meteoritics and Planetary Science*, 479 – 486, 2002.

Chappelow, J. E., V. L. Sharpton, S.E. Pitiss, and M.B. Kettner, Aeolian Activity within the Northeastern Portion of the Hematite Region: Evidence from the Analysis of Small Impact Craters, in *Lunar Planet. Sci., XXXIII*, Abstract #1798, Lunar and Planetary Institute, Houston (CD-ROM), 2002.

Christensen, P. R., J. L. Bandfield, R. N. Clark, K.S. Edgett, and V. E. Hamilton, Detection of crystalline hematite mineralization on Mars by the thermal emission spectrometer: evidence for near-surface water, *J. Geophys. Res.*, 105(E4), 9623-9642, 2000.

Crater Analysis Techniques Working Group, Standard techniques for presentation and analysis of crater size-frequency data, *Icarus*, 37, 467-474, 1979.

Gilmore, M. S., and K. L. Tanaka, Crater counts of MOC images within the Mars Exploration Rover Sinus Meridiani (Hematite Site) landing ellipses, in *Lunar Planet. Sci., XXXIII*, Abstract #1881, Lunar and Planetary Institute, Houston (CD-ROM), 2002.

Hartmann, W. K., Relative crater production rates on planets, *Icarus*, 31, 260 – 276, 1977.

Hartmann, W. K., M. Malin, A. McEwen, M. Carr, L. Soderblom, P. Thomas, E. Danielson, P. James, and J. Veverka, Evidence for recent volcanism on Mars from Crater counts, *Nature*, 397, 586-589, 1999.

Hartmann, W. K., Recent results from Mars Global Surveyor affecting landing site selection and habitats for past or present biological activity, *First landing site workshop for MER 2003*, #9019, 2001a.

Hartmann, W. K., J. Anguita, M. de la Casa, D. C. Berman, and E. Ryan, Martian Cratering 7: The role of impact gardening, *Icarus*, 149, 37-53, 2001b.

Hartmann, W. K., Introduction to Cratering Studies, http://www.psi.edu/projects/mgs/cratering.html, 25-Sep-2002.

Hartmann, W. K., Martian Cratering 8: Isochron refinement and the chronology of Mars, preprint submitted to *Icarus*, 2004.

Hynek, B. M., R. E. Arvidson, and R. J. Phillips, Geologic setting and origin of Terra Meridiani hematite deposit on Mars, *J. Geophys. Res.*, 107(E10), 5088, doi: 10.1029/2002JE001891, 2002.

Kargel, J.S., and R.G. Strom, Global Climatic Change on Mars, *Scientific American, Inc.*, November 1996.

Kelsey, C., Hartmann, W. K., Grier, J. A., and Berman, D. C., Observations of a hematite-rich region within Sinus Meridiani, in *Lunar Planet. Sci., XXXI*, Abstract #1524, Lunar and Planetary Institute, Houston (CD-ROM), 2000.

Kirkland L. E., K. C. Herr, P. M. Adams, A different perspective for the Mars rover "Opportunity" site: Fine-grained, consolidated hematite and hematite coatings, *Geophys. Res. Lett.*, 31, L05704, doi:10.1029/2003GL019284, 2004.

Lane, M.D., R.V. Morris, and P.R. Christensen, An extensive deposit of crystalline hematite in Terra Meridiani, Mars, in *Lunar Planet. Sci., XXX*, Abstract #1469, Lunar and Planetary Institute, Houston (CD-ROM), 1999.

Lane, M. D., R. V. Morris, S. A. Mertzman, and P. R. Christensen, Evidence for platy hematite grains in Sinus Meridiani, Mars, *J. Geophys. Res.*, 107(E12), 5126, doi:10.1029/2001JE001832, 2002.

Malin, M. C., M. H. Carr, G. E. Danielson, M. E. Davies, W. K. Hartmann, A. P. Ingersoll, P. B. James, H. Masursky, A. S. McEwen, L. A. Soderblom, P. Thomas, J. Veverka, M. A. Caplinger, M. A. Ravine, T. A. Soulanille, and J. L. Warren, Early views of the martian surface from the Mars Orbiter Camera of Mars Global Surveyor, *Science, 279,* 1681-1685, 1998.

McEwen, A.S., Secondary cratering on Mars: implications for age dating and surface properties, in *Proc. Sixth International Conference on Mars*, Abstract #3268, Lunar and Planetary Institute, 2003.

Melosh, H.J., *Impact Cratering: A Geologic Process*, 245 pp., Oxford University Press, 1989.

Noreen, E., K.L.Tanaka, and M.G. Chapman, TES Hematite Landing Sites in Sinus Meridiani for 2003 Mars Exploration Rover, *First landing site workshop for MER 2003*, #9014, 2001.

Opik, E. J., The Martian Surface, *Science*, V. 153, Issue 3733, 255-265, 1966.

Scott, D. H., and K. L. Tanaka, Geologic map of the western equatorial region of Mars, *U.S. Geol. Surv. Misc. Invest. Map, I-1802-A,* 1986.

Shoemaker, E.M., Exploration of the moon's surface, *American Scientist*, v. 50, no. 1, p. 99-130, 1962.

Squyres, S. W., R. E. Arvidson, J. F. Bell, III, J. Brückner, N. A. Cabrol, W. Calvin, M. H. Carr, P. R. Christensen, B. C. Clark, L. Crumpler, D. J. Des Marais, C. d'Uston, T. Economou, J. Farmer, W. Farrand, W. Folkner, M. Golombek, S. Gorevan, J. A. Grant, R. Greeley, J. Grotzinger, L. Haskin, K. E. Herkenhoff, S. Hviid, J. Johnson, G. Klingelhöfer, A. H. Knoll, G. Landis, M. Lemmon, R. Li, M. B. Madsen, M. C. Malin, S. M. McLennan, H. Y. McSween, D. W. Ming, J. Moersch, R. V. Morris, T. Parker, J. W. Rice, Jr., L. Richter, R. Rieder, M. Sims, M. Smith, P. Smith, L. A. Soderblom, R. Sullivan, H. Wänke, T. Wdowiak, M. Wolff, and A. Yen, The Opportunity Rover's Athena Science Investigation at Meridiani Planum, Mars, *Science*, 306, 1698-1703, doi: 10.1126/science.1106171, 2004.

Tanaka, K. L., Mars Pathfinder landing site: regional geology and mass-flow interpretation, in *Lunar Planet. Sci., XXIX*, Abstract #1800, Lunar and Planetary Institute, Houston (CD-ROM), 1998.

Appendix A

The following equations are the code used in Matlab created by John Chappelow (PhD candidate, UAF) to define the rim of a crater based on selecting three points upon its rim. Essentially, any three points define a circle and this program gets the center coordinates and radius of a circle defined by those 3 points. The radius is then doubled and used for cratering statistics.

R_1, R_2, and R_3 are the squares of the distances of each point from the point (0,0):

$$\begin{aligned} R_1 &= x_1^2 + y_1^2 \\ R_2 &= x_2^2 + y_2^2 \\ R_3 &= x_3^2 + y_3^2 \end{aligned} \tag{A1}$$

where the three points on the crater rim as entered by the user are x_1, y_1; x_2, y_2; and x_3, y_3.

The following is the equations of the coefficient matrices A and b:

$$\text{(A2)}\ A = \begin{bmatrix} x_2 - x_1 & y_2 - y_1 \\ x_3 - x_2 & y_3 - y_2 \end{bmatrix} \qquad \text{(A3)}\ b = \begin{bmatrix} \frac{R_2 - R_1}{2} \\ \frac{R_3 - R_2}{2} \end{bmatrix}$$

To solve this system of equations:

$$xy = inv(A) * b \tag{A4}$$

$$r = \sqrt{(xy(1) - x_1)^2 + (xy(2) - y_1)^2} \tag{A5}$$

$$D = r * 2 \tag{A6}$$

The column vector xy contains the coordinates of the circle's center, r is the circle's radius, and D is its diameter.